Computer Methods in Applied Mechanics and Engineering 432 (2024) 117354

Contents lists available at ScienceDirect

Comput. Methods Appl. Mech. Engrg.

journal homepage: www.elsevier.com/locate/cma

Mixed displacement–pressure formulations and suitable finite elements for multimaterial problems with compressible and incompressible models

Chennakesava Kadapa

School of Computing, Engineering and the Built Environment, Edinburgh Napier University, Edinburgh EH10 5DT, United Kingdom

ARTICLE INFO

Keywords:
Finite element method
Hyperelasticity
Incompressibility
Mixed formulation
Stress discontinuity

ABSTRACT

Multimaterial problems in linear and nonlinear elasticity are some of the least explored using mixed finite element formulations with higher-order elements. The fundamental issue in adapting the mixed displacement–pressure formulations with linear and higher-order continuous elements for the pressure field is their inability to capture pressure and stress jumps across material interfaces. In this paper, for the first time in literature, we perform comprehensive studies of multimaterial problems in elasticity consisting of compressible and incompressible material models using the mixed displacement–pressure formulation to assess the performance of different element types in accurately resolving pressure fields within the domains and pressure jumps across material interfaces. In particular, inf–sup stable displacement–pressure combinations with element-wise discontinuous pressure for triangular and tetrahedral elements are considered and their performance is assessed along with the Q1/P0 element and Taylor–Hood elements using several numerical examples. The results show that Taylor–Hood elements fail to capture the stress jumps due to the continuity of DOFs across elements, the Crouzeix–Raviart (P2b/P1dc) element yields substantially poor pressure fields despite a significant increase in pressure degrees of freedom and that the P3/P1dc element produces superior quality results fields when compared with the P2b/P1dc element.

1. Introduction

Elasticity problems consisting of multiple materials are ubiquitous in nature, e.g., biological tissues and man-made composites. For rubber-like polymers and soft tissues, the stress–strain relation is defined by hyperelastic models, which also form the building blocks for the constitutive relations for soft multifunctional composites such as electroactive polymers [1], magnetoactive polymers [2], hydrogels [3], etc. The typical deformation behaviour of materials, in general, can range from the compressible regime with significant volumetric changes to the incompressible regime with zero volumetric change.

While compressible materials are relatively straightforward to simulate using pure displacement formulations, incompressible hyperelastic models require sophisticated finite element formulations for computing accurate numerical results. Formulations such as ***F***-bar formulation [4], average nodal strain formulation [5], reduced integration method with hourglass control [6], enhanced-strain method [7], enhanced assumed strain (EAS) methods [8], energy-sampling stabilisation [9], smoothed FEM [10–12] etc., that take the contribution from the volumetric part of the strain energy function into the stiffness matrix end up being computationally expensive due to the increased ill-conditioning of the resulting stiffness matrix as the incompressibility limit is approached, that is,

---

E-mail address: c.kadapa@napier.ac.uk.

https://doi.org/10.1016/j.cma.2024.117354
Received 16 May 2024; Received in revised form 22 July 2024; Accepted 2 September 2024

as Poisson's ratio approaches 0.5. For simulating the truly incompressible material models accurately, mixed displacement–pressure formulation, also referred to as the hybrid formulation, is the only viable option.

In the mixed displacement–pressure formulation, the pressure field acts as a Lagrange multiplier for enforcing the incompressibility constraint [13–17]. Other variants of mixed formulations formulate the problem by adding the difference in pressure as a least-squares term to the total potential energy [18]. To overcome the issues with solving the saddle-point matrices resulting from the mixed displacement–pressure formulation and also enable the use of equal-order interpolation for the displacement and pressure fields, pressure-stabilised formulations inspired by the developments in computational fluid dynamics have been adapted for elasticity problems [19–35]. Recent efforts on mixed displacement–volumetric strain formulation [36,37] follow similar stabilisation to overcome volumetric locking.

The majority of mixed displacement–pressure formulations with *inf–sup* stable elements such as Taylor–Hood (P2/P1 and Q2/Q1) elements [13,38] and Bézier family [16], subdivision stabilised NURBS elements [15], and mixed stabilised formulations [19,24,27], have been studied extensively for problems with a single material. However, problems of practical interest often consist of multiple materials, requiring numerical methods that are applicable to such problems. A fundamental requirement in simulating solid mechanics problems with multiple materials is accurately capturing the stress discontinuities across material interfaces. While the mixed displacement–pressure formulation with the Q1/P0 element (linear quadrilateral/hexahedral for displacement and element-wise constant for pressure) is readily applicable to multimaterial problems, higher-order elements are not so readily adaptable for problems with multiple materials. Although the Taylor–Hood family of elements satisfy the *inf–sup* stability condition, their straightforward applicability is limited to incompressible solid mechanics problems with a single material. For multi-material problems, direct application of the Taylor–Hood elements results in incorrect pressure (and hence stress) values at the material interfaces. This is due to the continuity of pressure degrees of freedom (DOFs) across elements, which makes it impossible to capture pressure (and hence stress) jumps at material interfaces without additional effort.

To accurately resolve pressure jumps at the material interfaces using linear or higher-order elements for pressure, the pressure DOFs for the elements sharing a material interface must be duplicated, as done in Kadapa et al. [3]. However, such an approach of duplicating pressure DOFs is only possible to implement with knowing the additional information, such as the area/volume the element is attached to. Note that we cannot prepare the duplicate nodes based on the material information alone, as disjointed locations can share the same material number, for example, particles distributed in a matrix. Moreover, the approach of duplication of pressure DOFs is challenging to implement in parallel codes for distributed memory architectures based on a message-passing interface; this requires a significant amount of data transfer among processes. An alternative is to generate non-matching meshes for each component, but this requires a contact formulation to enforce the displacement continuity, which adds unnecessary overhead. Therefore, pressure spaces must be discontinuous to accurately resolve the pressure jumps across material interfaces.

Although the well-known Q1/P0 element [17,39] is readily adaptable to such problems, its lack of *inf–sup* stability and lower-order nature forces one to use extremely finer meshes for accurate results [1]. Among higher-order elements with discontinuous pressure spaces, the Crouzeix–Raviart element (P2b/P1dc - quadratic triangular/tetrahedral element with a cubic bubble for displacements and linear element-wise discontinuous space for pressure) [40–42] and P3/P1dc element (cubic triangular/tetrahedral element for displacements and linear element-wise discontinuous space for pressure) [42,43] are of particular interest because they allow for the easy of generation of triangular and tetrahedral meshes for complex geometries. However, these elements have not been explored in the context of nonlinear elasticity problems. Motivated by the need to accurately simulate nonlinear elasticity problems consisting of multiple materials of which one or all materials are incompressible, in this work, we evaluate the accuracy and performance of P2b/P1dc and P3/P1dc elements in the context of linear and nonlinear elasticity problems, particularly those made up multiple materials, for the first time in literature to the best of our knowledge. The accuracy of results is evaluated by calculating error norms for the examples of thick-walled cylinders and spheres made of linear elastic materials and subjected to internal pressure. The performance of the elements is further demonstrated by studying benchmark examples and their extensions in nonlinear elasticity with hyperelastic materials.

2. Kinematics, strain and stress measures and constitutive relations

We consider an arbitrary solid body with $\mathcal{B}_0$ as the reference configuration and $\mathcal{B}_t$ as the current configuration the body assumes under the action of external loads. A nonlinear deformation map $\mathcal{X} : \mathcal{B}_0 \rightarrow \mathcal{B}_t$ takes the point $\boldsymbol{X}$ in the reference configuration, $\mathcal{B}_0$, to the point $\boldsymbol{x}$ in the current configuration, $\mathcal{B}_t$, so that the displacement is $\boldsymbol{u} = \boldsymbol{x} - \boldsymbol{X}$. Assuming that the map $\mathcal{X}$ is smooth and invertible so that the deformation gradient $\boldsymbol{F}$ is well defined. $\boldsymbol{F}$ and its determinant J are given as

$$\boldsymbol{F} := \frac{\partial \mathcal{X}}{\partial \boldsymbol{X}} = \frac{\partial \boldsymbol{x}}{\partial \boldsymbol{X}} = \boldsymbol{I} + \frac{\partial \boldsymbol{u}}{\partial \boldsymbol{X}}, \qquad J := \det(\boldsymbol{F}), \tag{1}$$

where $\boldsymbol{I}$ is the second-order identity tensor.

The right Cauchy–Green deformation tensor, $\boldsymbol{C}$, the Green–Lagrange strain tensor, $\boldsymbol{E}$, and the infinitesimal strain tensor, $\boldsymbol{\varepsilon}$, are defined as

$$\boldsymbol{C} = \boldsymbol{F}^{\mathrm{T}}\,\boldsymbol{F}, \tag{2}$$

$$\boldsymbol{E} = \frac{1}{2}\,[\boldsymbol{C} - \boldsymbol{I}], \tag{3}$$

$$\boldsymbol{\varepsilon} = \frac{1}{2}\left[(\nabla \boldsymbol{u})^{\mathrm{T}} + \nabla \boldsymbol{u}\right]. \tag{4}$$

In the case of truly incompressible materials in the finite strain regime, the deformation of the solid is such that the total volume change at any point in the domain is zero. This acts as a constraint on the displacement field that needs to be solved in the elasticity problem. Mathematically, the *incompressibility constraint* in the finite strain regime is given as,

$$J = 1. \tag{5}$$

To model hyperelastic materials in the incompressible finite strain regime, the deformation gradient is decomposed into deviatoric and volumetric components as

$$\boldsymbol{F} = \boldsymbol{F}_{\text{vol}}\,\boldsymbol{F}_{\text{dev}}, \tag{6}$$

where

$$\boldsymbol{F}_{\text{vol}} := J^{1/3}\,\boldsymbol{I}, \quad \text{and} \quad \boldsymbol{F}_{\text{dev}} := J^{-1/3}\boldsymbol{F}, \tag{7}$$

and the modified version of the deformation gradient is defined as

$$\overline{\boldsymbol{F}} := J^{-1/3}\,\boldsymbol{F}. \tag{8}$$

Accordingly, the modified versions of the right Cauchy–Green tensor and the Green–Lagrange strain tensors are given as

$$\overline{\boldsymbol{C}} := \overline{\boldsymbol{F}}^{\mathrm{T}}\,\overline{\boldsymbol{F}} \tag{9}$$

$$\overline{\boldsymbol{E}} : \frac{1}{2}\left[\overline{\boldsymbol{C}} - \boldsymbol{I}\right] \tag{10}$$

The nonlinear behaviour of soft polymers and soft biological tissues is defined by using hyperelastic models in the form of strain energy density functions. For nearly incompressible materials, the strain energy functions for hyperelastic models are assumed to be split into deviatoric and volumetric parts as,

$$\Psi(\overline{\boldsymbol{C}}, J) = \Psi^{\text{dev}}(\overline{\boldsymbol{C}}) + \Psi^{\text{vol}}(J). \tag{11}$$

A wide variety of functions for deviatoric and volumetric are available in the literature. In this work, Neo-Hookean and Mooney–Rivlin models are considered for the deviatoric part.

3. Mixed displacement–pressure formulation in small strains

In this work, the mixed formulation in small strains is tuned for linear isotropic elastic materials. For the mixed displacement–pressure formulation in small strains, the infinitesimal strain tensor is decomposed into deviatoric and volumetric parts as

$$\boldsymbol{\varepsilon} = \boldsymbol{\varepsilon}_{\text{dev}} + \boldsymbol{\varepsilon}_{\text{vol}} = \bar{\boldsymbol{\varepsilon}} + \boldsymbol{\varepsilon}_{\text{vol}} \tag{12}$$

with

$$\boldsymbol{\varepsilon}_{\text{vol}} = \varepsilon_{MM}\,\boldsymbol{I} = u_{M,M}\,\boldsymbol{I}, \tag{13}$$

$$\bar{\boldsymbol{\varepsilon}} = \boldsymbol{\varepsilon}_{\text{dev}} = \boldsymbol{\varepsilon} - \frac{1}{3}\,u_{M,M}\,\boldsymbol{I} \tag{14}$$

where the subscripts I, J and M denote the coordinate components, and the repeated index means summation. For example, $\varepsilon_{MM} = u_{M,M} = \frac{\partial u_X}{\partial X} + \frac{\partial u_Y}{\partial Y} + \frac{\partial u_Z}{\partial Z}$.

With p as the additional unknown, the Cauchy stress for linear elastic material for the mixed formulation is calculated as

$$\boldsymbol{\sigma} = \bar{\boldsymbol{\sigma}} + p\,\boldsymbol{I} = 2\,\mu\,\bar{\boldsymbol{\varepsilon}} + p\,\boldsymbol{I} \tag{15}$$

and in component form as

$$\sigma_{IJ} = \overline{\sigma}_{IJ} + p\,\delta_{IJ} = 2\,\mu\,\overline{\varepsilon}_{IJ} + p\,\delta_{IJ} \tag{16}$$

For compressible materials ($\nu < 0.5$), hydrostatic pressure, p, is related to the volumetric strain via the relation

$$p = \kappa\,\varepsilon_v \tag{17}$$

where κ is the bulk modulus. For incompressible materials, p acts as a Lagrange multiplier enforcing the volumetric constraint

$$\varepsilon_v = 0. \tag{18}$$

Considering both compressible and incompressible materials, the total potential energy for the mixed displacement–pressure formulation in small strains can be written as

$$\Pi(\boldsymbol{u}, p) = \int_{\mathcal{B}_0} \left[\frac{1}{2}\,\nabla\boldsymbol{u}^{\mathrm{T}}\,\bar{\boldsymbol{\sigma}} + p\,[\varepsilon_v - \frac{p}{2\kappa}]\right] \mathrm{d}V - \Pi_{\text{ext}}, \tag{19}$$

where

$$\Pi_{\text{ext}} = \int_{\mathcal{B}_0} \boldsymbol{u}^{\mathrm{T}} \boldsymbol{f}_0 \, \mathrm{d}V + \int_{\partial \mathcal{B}_0^{\mathrm{N}}} \boldsymbol{u}^{\mathrm{T}} \boldsymbol{t}_0 \, \mathrm{d}A, \tag{20}$$

is the energy contribution from the external body force, $\boldsymbol{f}_0$, and traction, $\boldsymbol{t}_0$.

Following the variational calculus, the first variation ($\delta()$) and second variation ($d()$) of Π are

$$\delta\Pi = \int_{\mathcal{B}_0} \left[\delta u_{I,J} \, \bar{\sigma}_{IJ} + \delta u_{I,J} \, p \, \delta_{IJ} + \delta p \, u_{M,M} - \frac{p}{\kappa} \, \delta p \right] - \delta \Pi_{\text{ext}} \tag{21}$$

$$d(\delta\Pi) = \int_{\mathcal{B}_0} \left[\delta u_{I,J} \, \mathbb{C}_{IJKL} \, du_{K,L} + \delta u_{I,J} \, \delta_{IJ} \, dp + \delta p \, \delta_{KL} \, du_{K,L} - \frac{1}{\kappa} \, \delta p \, dp \right] \tag{22}$$

where

$$\mathbb{C}_{IJKL} = \frac{\partial \bar{\sigma}_{IJ}}{\partial u_{K,L}} = \mu \, \delta_{IK} \, \delta_{JL} + \mu \, \delta_{IL} \, \delta_{JK} - \frac{2}{3} \, \mu \, \delta_{IJ} \, \delta_{KL}, \tag{23}$$

is the fourth-order elasticity tensor.

Using the finite element approximations for the solution variables and their variations,

$$\boldsymbol{u} = \mathbf{N}_{\boldsymbol{u}} \, \mathbf{u}, \qquad p = \mathbf{N}_p \, \mathbf{p}, \tag{24}$$

$$\delta\boldsymbol{u} = \mathbf{N}_{\boldsymbol{u}} \, \delta\mathbf{u}, \qquad \delta p = \mathbf{N}_p \, \delta\mathbf{p}, \tag{25}$$

where $\mathbf{N}_{\boldsymbol{u}}$ and $\mathbf{N}_p$ are the basis functions, respectively, for the displacement and pressure fields, and $\mathbf{u}$ and $\mathbf{p}$, respectively, are the nodal degrees of freedom (DOFs), respectively, for the displacement and pressure fields, the coupled matrix system for the mixed formulation can be written as

$$\begin{bmatrix} \mathbf{K}_{\boldsymbol{uu}} & \mathbf{K}_{\boldsymbol{u}p} \\ \mathbf{K}_{p\boldsymbol{u}} & \mathbf{K}_{pp} \end{bmatrix} \begin{Bmatrix} \mathbf{u} \\ \mathbf{p} \end{Bmatrix} = \begin{Bmatrix} \mathbf{F}_{\boldsymbol{u}} \\ \mathbf{0} \end{Bmatrix} \tag{26}$$

where

$$\mathbf{K}_{\boldsymbol{uu}} = \int_{\mathcal{B}_0} \mathbf{G}_0^{\mathrm{T}} \, \mathbf{C} \, \mathbf{G}_0 \, \mathrm{d}V, \tag{27a}$$

$$\mathbf{K}_{\boldsymbol{u}p} = \int_{\mathcal{B}_0} \mathbf{D}_0^{\mathrm{T}} \, \mathbf{N}_p \, \mathrm{d}V = \mathbf{K}_{p\boldsymbol{u}}^{\mathrm{T}} \tag{27b}$$

$$\mathbf{K}_{pp} = -\int_{\mathcal{B}_0} \frac{1}{\kappa} \, \mathbf{N}_p^{\mathrm{T}} \, \mathbf{N}_p \, \mathrm{d}V \tag{27c}$$

$$\mathbf{F}_{\boldsymbol{u}} = \mathbf{F}^{\text{ext}} = \int_{\mathcal{B}_0} \mathbf{N}_{\boldsymbol{u}}^{\mathrm{T}} \, \boldsymbol{f}_0 \, \mathrm{d}V + \int_{\partial \mathcal{B}_0^{\mathrm{N}}} \mathbf{N}_{\boldsymbol{u}}^{\mathrm{T}} \, \boldsymbol{t}_0 \, \mathrm{d}A, \tag{27d}$$

where $\mathbf{C}$ is the fourth-order elasticity tensor ($\mathbb{C}$) expressed in the matrix form. $\mathbf{G}_0$ and $\mathbf{D}_0$ are the gradient–displacement and divergence–displacement matrices with respect to the reference configuration, which, for a single basis function, $N_{\boldsymbol{u}}$, are given as

$$\mathbf{G}_0 = \begin{bmatrix} \frac{\partial N_{\boldsymbol{u}}}{\partial X} & 0 & 0 & \frac{\partial N_{\boldsymbol{u}}}{\partial Y} & 0 & 0 & \frac{\partial N_{\boldsymbol{u}}}{\partial Z} & 0 & 0 \\ 0 & \frac{\partial N_{\boldsymbol{u}}}{\partial X} & 0 & 0 & \frac{\partial N_{\boldsymbol{u}}}{\partial Y} & 0 & 0 & \frac{\partial N_{\boldsymbol{u}}}{\partial Z} & 0 \\ 0 & 0 & \frac{\partial N_{\boldsymbol{u}}}{\partial X} & 0 & 0 & \frac{\partial N_{\boldsymbol{u}}}{\partial Y} & 0 & 0 & \frac{\partial N_{\boldsymbol{u}}}{\partial Z} \end{bmatrix}^{\mathrm{T}}, \tag{28}$$

$$\mathbf{D}_0 = \begin{bmatrix} \frac{\partial N_{\boldsymbol{u}}}{\partial X} & \frac{\partial N_{\boldsymbol{u}}}{\partial Y} & \frac{\partial N_{\boldsymbol{u}}}{\partial Z} \end{bmatrix}. \tag{29}$$

4. Mixed displacement–pressure formulation in finite strains

We adapt the mixed displacement–pressure formulation that is recently proposed by Kadapa and Hossain [17] because of its advantage in yielding symmetric global stiffness matrices irrespective of the volumetric energy function. Following Kadapa and Hossain [17], the total energy functional for the mixed displacement–pressure formulation in the finite strain regime is given as,

$$\Pi(\boldsymbol{u}, p) = \int_{\mathcal{B}_0} \left[\Psi^{\text{dev}}(\overline{\boldsymbol{C}}) + \Psi_p(J, p) \right] \mathrm{d}V - \Pi_{\text{ext}}, \tag{30}$$

where Ψ_p is the generic energy functional that accounts for the effect of volumetric deformation in the compressible as well as incompressible regime while considering arbitrary volumetric energy function. Ψ_p enforces the incompressibility constraint $J{=}1$ using the Lagrange multiplier approach for the truly incompressible case while it uses a more generic constraint by incorporating the volumetric energy function Ψ^{vol} [17]. For the generic case, we have $\Psi_p(J, p)$ in the perturbed Lagrangian form as

$$\Psi_p(J, p) = p \left[J - \widehat{J} - \frac{\widehat{\vartheta} \, p}{2} \right] \tag{31}$$

with p as the Lagrange multiplier. $\widehat{J}$ and $\widehat{\vartheta}$ are calculated using

$$\widehat{J} = J_n - \frac{\left.\dfrac{\partial \Psi^{\text{vol}}(J)}{\partial J}\right|_{J_n}}{\left.\dfrac{\partial^2 \Psi^{\text{vol}}(J)}{\partial J^2}\right|_{J_n}}; \qquad \widehat{\vartheta} = \frac{1}{\left.\dfrac{\partial^2 \Psi^{\text{vol}}(J)}{\partial J^2}\right|_{J_n}}, \tag{32}$$

with $J_{\bullet} = \det(\boldsymbol{F}(\boldsymbol{u}_{\bullet}))$. The subscript n in Eq. (32) denotes the previously converged load step. From the generic case in (31), we can recover the truly incompressible case by setting $\widehat{J} = 1$ and $\widehat{\vartheta} = 0$ based on the user input. The reader is referred to Kadapa and Hossain [17] for the comprehensive details on the mixed formulation and its demonstrated advantages using benchmark numerical examples.

By taking the first variation (δ) of the total energy functional given in Eq. (30), we get

$$\delta\Pi = \int_{\mathcal{B}_0} \left[\delta u_{i,j} \left[\overline{\sigma}_{ij} + p\,\delta_{ij} \right] J + \delta p \left[J - \widehat{J} - \widehat{\vartheta}\,p \right] \right] \mathrm{d}V - \delta\,\Pi_{\text{ext}}. \tag{33}$$

Using the finite element approximations for the displacement and pressure fields and their variations in (24), the semi-discrete form for the mixed formulation in finite strains can be written as,

$$\mathbf{R}_{u} = \int_{\mathcal{B}_t} \mathbf{G}^{\mathrm{T}}\,\boldsymbol{\sigma}\,\mathrm{d}v - \mathbf{F}^{\text{ext}} = \mathbf{0}, \tag{34a}$$

$$\mathbf{R}_{p} = \int_{\mathcal{B}_0} \mathbf{N}_p^{\mathrm{T}} \left[J - \widehat{J} - \widehat{\vartheta}\,p \right] \mathrm{d}V = \mathbf{0}, \tag{34b}$$

where $\boldsymbol{\sigma}$ is the total stress and discrete gradient–displacement matrix with respect to the current configuration ($\mathbf{G}$) for a single basis function is given as

$$\mathbf{G} = \begin{bmatrix} \frac{\partial N_{\boldsymbol{u}}}{\partial x} & 0 & 0 & \frac{\partial N_{\boldsymbol{u}}}{\partial y} & 0 & 0 & \frac{\partial N_{\boldsymbol{u}}}{\partial z} & 0 & 0 \\ 0 & \frac{\partial N_{\boldsymbol{u}}}{\partial x} & 0 & 0 & \frac{\partial N_{\boldsymbol{u}}}{\partial y} & 0 & 0 & \frac{\partial N_{\boldsymbol{u}}}{\partial z} & 0 \\ 0 & 0 & \frac{\partial N_{\boldsymbol{u}}}{\partial x} & 0 & 0 & \frac{\partial N_{\boldsymbol{u}}}{\partial y} & 0 & 0 & \frac{\partial N_{\boldsymbol{u}}}{\partial z} \end{bmatrix}^{\mathrm{T}}. \tag{35}$$

We use the Newton–Raphson scheme to solve the set of nonlinear Eqs. (34a) and (34b) in an efficient manner. With $n+1$ and n denoting the current and previously converged load steps, respectively, and $k+1$ and k denoting the current and previous iterations at the current load step, the displacement DOFs, $\mathbf{u}_{n+1}$, and pressure DOFs, $\mathbf{p}_{n+1}$, at the current iteration of the current load step are computed as the iterative increments, $\overline{\Delta}\mathbf{u}$ and $\overline{\Delta}\mathbf{p}$, from the respective quantities at the previous iteration, $\mathbf{u}_{n+1}^{(k)}$ and $\mathbf{p}_{n+1}^{(k)}$, as

$$\mathbf{u}_{n+1}^{(k+1)} = \mathbf{u}_{n+1}^{(k)} + \overline{\Delta}\mathbf{u}, \tag{36a}$$

$$\mathbf{p}_{n+1}^{(k+1)} = \mathbf{p}_{n+1}^{(k)} + \overline{\Delta}\mathbf{p}, \tag{36b}$$

By adapting the Newton–Raphson scheme, we arrive at the coupled matrix system given as

$$\begin{bmatrix} \mathbf{K}_{uu} & \mathbf{K}_{up} \\ \mathbf{K}_{pu} & \mathbf{K}_{pp} \end{bmatrix} \begin{Bmatrix} \overline{\Delta}\mathbf{u} \\ \overline{\Delta}\mathbf{p} \end{Bmatrix} = - \begin{Bmatrix} \mathbf{R}_{u} \\ \mathbf{R}_{p} \end{Bmatrix} \tag{37}$$

where

$$\mathbf{K}_{uu} = \int_{\mathcal{B}_t} \mathbf{G}^{\mathrm{T}}\,\mathbf{e}(\boldsymbol{u}_{n+1}^{(k)}, p_{n+1}^{(k)})\,\mathbf{G}\,\mathrm{d}v, \tag{38a}$$

$$\mathbf{K}_{up} = \int_{\mathcal{B}_t} \mathbf{D}^{\mathrm{T}}\,\mathbf{N}_p\,\mathrm{d}v = \mathbf{K}_{pu}^{\mathrm{T}} \tag{38b}$$

$$\mathbf{K}_{pp} = -\int_{\mathcal{B}_0} \widehat{\vartheta}\,\mathbf{N}_p^{\mathrm{T}}\,\mathbf{N}_p\,\mathrm{d}V \tag{38c}$$

$$\mathbf{R}_{u} = \int_{\mathcal{B}_t} \mathbf{G}^{\mathrm{T}}\,\boldsymbol{\sigma}(\boldsymbol{u}_{n+1}^{(k)}, p_{n+1}^{(k)})\,\mathrm{d}v - \mathbf{F}_{n+1}^{\text{ext}}, \tag{38d}$$

$$\mathbf{R}_{p} = \int_{\mathcal{B}_0} \mathbf{N}_p^{\mathrm{T}} \left[J_{n+1}^{(k)} - \widehat{J} - \widehat{\vartheta}\,p_{n+1}^{(k)} \right] \mathrm{d}V, \tag{38e}$$

where $\mathbf{e}$ is material tangent tensor ($\mathbb{e}$) expressed in the matrix form and $\mathbf{D}$ is the divergence–displacement matrix with respect to the current configuration, which, for a single basis function, $N_{\boldsymbol{u}}$, is given as

$$\mathbf{D} = \begin{bmatrix} \frac{\partial N_{\boldsymbol{u}}}{\partial x} & \frac{\partial N_{\boldsymbol{u}}}{\partial y} & \frac{\partial N_{\boldsymbol{u}}}{\partial z} \end{bmatrix}. \tag{39}$$

Note that $\mathbf{K}_{uu}$ contains contributions from geometric and material nonlinearities.

Following the derivation above, the effective first Piola–Kirchhoff stress tensor ($\boldsymbol{P}$) for the mixed formulation is defined as

$$\boldsymbol{P} := \frac{\partial \Psi^{\text{dev}}(\overline{\boldsymbol{C}})}{\partial \boldsymbol{F}} + p\,J\,\boldsymbol{F}^{-\mathrm{T}} = \overline{\boldsymbol{P}} + p\,J\,\boldsymbol{F}^{-\mathrm{T}}. \tag{40}$$

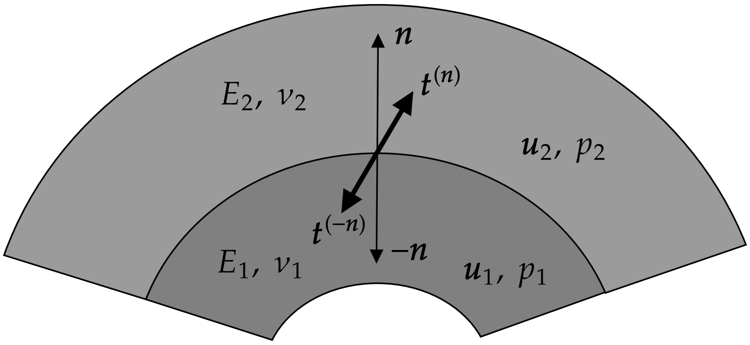

Fig. 1. A typical interface between two domains made of materials with different material properties.

In the above equation, deviatoric component of the first Piola–Kirchhoff stress tensor, $\overline{\boldsymbol{P}}$ is computed solely from the deviatoric part of the strain energy function, Ψ^{dev}. From $\boldsymbol{P}$, the Cauchy stress tensor becomes,

$$\boldsymbol{\sigma} := \frac{1}{J}\,\boldsymbol{P}\,\boldsymbol{F}^{\mathrm{T}} = \frac{1}{J}\,\overline{\boldsymbol{P}}\,\boldsymbol{F}^{\mathrm{T}} + p\,\boldsymbol{I}. \tag{41}$$

The material tangent tensor ($\mathbb{C}$) of order four is computed as

$$\mathbb{C}_{ijkl} = \frac{1}{J}\,F_{jJ}\,\frac{\partial \overline{P}_{iJ}}{\partial F_{kL}}\,F_{lL} + p\,\left[\delta_{ij}\,\delta_{lk} - \delta_{il}\,\delta_{jk}\right]. \tag{42}$$

4.1. Finite element spaces

It is well-established that the finite element spaces for the displacement and pressure for the mixed formulation cannot be chosen arbitrarily [41]. The combination of displacement–pressure spaces must satisfy the *inf–sup* condition, and a pressure space that is not *inf–sup* compatible with the displacement space yields spurious oscillations in the pressure field. Because of this restriction, the number of such spaces for the displacement–pressure combination is limited. Among the class of finite elements that satisfy the *inf–sup* condition, Taylor–Hood elements such as P2/P1, Q2/Q1, and their higher-order extensions are popular. Recently, their extensions to NURBS [15] and Bézier elements, e.g., BT2/BT1, BQ2/BQ1 and BW2/BW1 [16,44] have also been proposed. Among the elements that do not satisfy the *inf–sup* condition, the Q1/P0 element is widely used because of its simplicity despite yielding a checkerboard pattern for pressure.

However, Taylor–Hood elements pose some serious issues when applied to problems with material interfaces. To understand this, let us consider a material interface between two domains with different material properties as shown in Fig. 1. The Young's moduli of the two domains are E_1 and E_2, and their respective Poisson's ratio are ν_1 and ν_2. The displacement and pressure fields for the first domain are $\boldsymbol{u}_1$ and p_1, respectively, and the corresponding quantities for the second domain are $\boldsymbol{u}_2$ and p_2. For the mixed displacement–pressure formulation, we can express the Cauchy stresses in the ith domain as

$$\boldsymbol{\sigma}_i = 2\,\mu_i\,\bar{\varepsilon}(\boldsymbol{u}_i) + p_i\,\boldsymbol{I}, \qquad for \qquad i = 1, 2. \tag{43}$$

The displacement field should be continuous at the interface for the perfectly bonded interface. Moreover, the Euler and Cauchy stress principle [45] mandates the continuity of tractions at the interface. The continuity of displacements is easily ensured by the C^0 continuity of the adapted Lagrange family of elements for the displacement field. But, continuity of tractions ($\boldsymbol{t}^{(\boldsymbol{n})} = -\boldsymbol{t}^{(-\boldsymbol{n})}$), as given by

$$2\,\mu_1\,\bar{\varepsilon}(\boldsymbol{u}_1)\cdot\boldsymbol{n} + p_1\,\boldsymbol{n} = 2\,\mu_2\,\bar{\varepsilon}(\boldsymbol{u}_2)\cdot\boldsymbol{n} + p_2\,\boldsymbol{n} \tag{44}$$

requires that the pressure fields p_1 and p_2 must be discontinuous across the interface. However, because of the C^0 continuity of pressure DOFs for the Taylor–Hood elements, to capture such discontinuities in the pressure field either the pressure DOFs at the interface must be duplicated [3], which is quite cumbersome for generic problems in 3D, or a suitable contact formulation must be employed if both displacement and pressure DOFs are duplicated or non-matching meshes are used, which adds unnecessary overhead. As an alternative, we propose elements with discontinuous pressure spaces.

In this work, we consider the Q1/P0 element, the P2/P1 element, the Crouzeix–Raviart (P2b/P1dc) element [40], and the P3/P1dc element. The P2b/P1dc element is a quadratic triangular/tetrahedral element enriched with a cubic bubble for the displacement (P2b) and element-wise linear discontinuous element (P1dc) for pressure. In the P3/P1dc element, the displacement field is approximated with cubic triangular/tetrahedral element and the pressure is approximated with element-wise linear discontinuous spaces. The displacement and pressure nodes for the different 2D elements considered in this work are illustrated in Fig. 2.

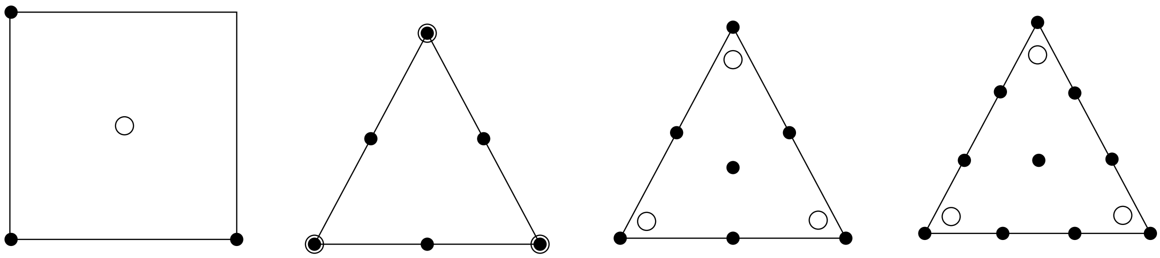

(a) Q1/P0 (b) P2/P1 (c) P2b/P1dc (d) P3/P1dc

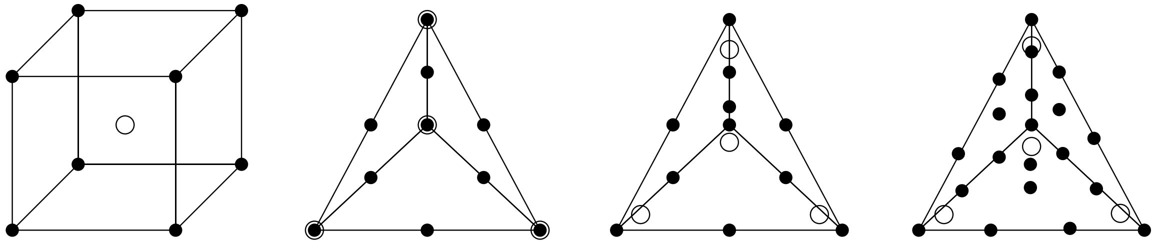

(e) Q1/P0 (f) P2/P1 (g) P2b/P1dc (h) P3/P1dc

Fig. 2. Different elements used. Markers • and ○, respectively, denote displacement and pressure nodes.

5. Numerical examples

We study the accuracy of Q1/P0, P2/P1, P2b/P1dc and P3/P1dc elements using several benchmark examples especially in nonlinear elasticity and compare their relative merits and issues. The formulations are implemented in an in-house code written in C++. The meshes are generated using GMSH [46] and the results are postprocessed using ParaView [47].

The strain energy functions considered in this work are given below.

- Neo-Hookean model

$$\Psi^{\text{dev}} = \frac{\mu}{2}\,\left[\bar{I}_1 - 3\right] \tag{45}$$

- Mooney–Rivlin model

$$\Psi^{\text{dev}} = C_{10}\,\left[\bar{I}_1 - 3\right] + C_{01}\,\left[\bar{I}_2 - 3\right] \tag{46}$$

- Volumetric energy function

$$\Psi^{\text{vol}} = \frac{\kappa}{2}\,[J-1]^2 \tag{47}$$

where μ is the shear modulus, κ is the bulk modulus, C_{01} and C_{10} are the material constants.

5.1. *Thick-walled cylinder under internal pressure*

In the first example, we consider a thick-walled cylinder subjected to internal pressure. The 2D model is assumed to be in plane-strain condition. In addition to the simple thick-walled cylinder made of a single material, see Fig. 3(a), we also consider a composite cylinder that is made of two different materials, see Fig. 3(b), to demonstrate the effectiveness of different element types in capturing the pressure fields and stress discontinuities at the material interfaces. The radii of the circular portions are $r_i = 100$ mm, $r_0 = 200$ mm and $r_m = 150$ mm. The material properties are: $E = 200$ MPa, $\nu = \{0.3, 0.5\}$, and $E_1 = 200$ MPa, $E_2 = 20$ MPa and $\nu_1 = \nu_2 = \{0.3, 0.5\}$. The pressure on the inner surface of the cylinder is $p_i = 0.1$ MPa. Since the condensed form of Q1/P0 is not applicable to perfectly incompressible cases, Poisson's ratio for the Q1/P0 element is taken as 0.4999. The analytical solutions are provided in Appendix.

5.1.1. *Simple thick-walled cylinder*

Convergence analysis is conducted with five uniform meshes shown in Fig. 4. Graphs of L_2 relative error norms in displacement, pressure and stress against mesh refinement are shown in Figs. 5 and 6, respectively, for $\nu = 0.3$ and $\nu = 0.5$. As shown, all four element types considered in the study yield the expected convergence rates. A closer look at the convergence rates and the magnitude

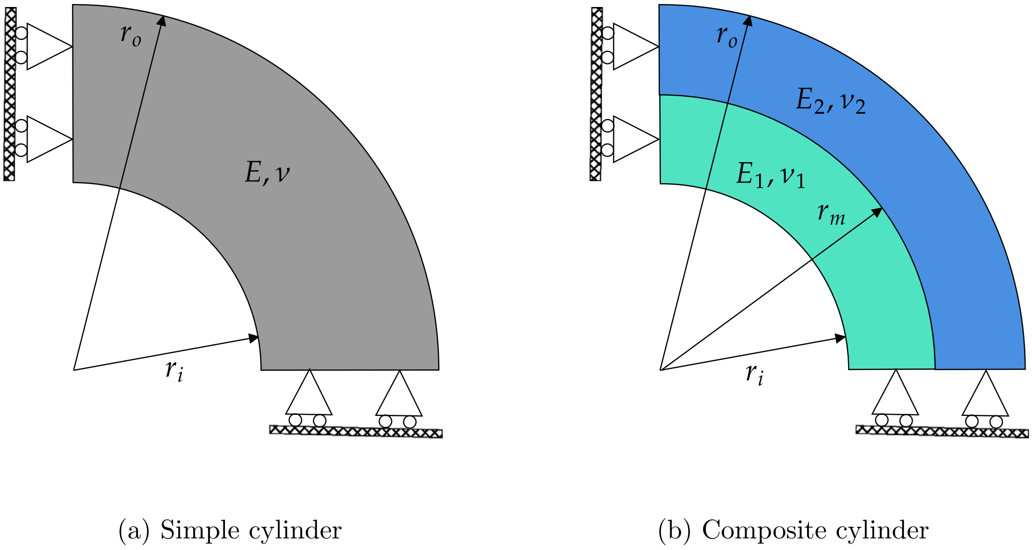

(a) Simple cylinder (b) Composite cylinder

Fig. 3. Thick-walled cylinder: problem setup for simple and composite cylinders.

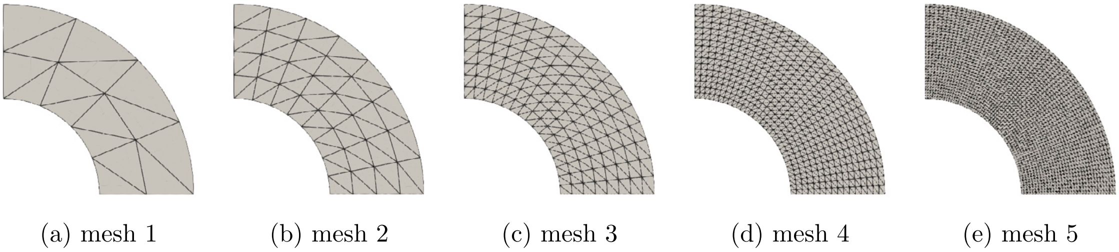

(a) mesh 1 (b) mesh 2 (c) mesh 3 (d) mesh 4 (e) mesh 5

Fig. 4. Simple thick-walled cylinder: meshes used for the analysis.

of errors reveals a surprising outcome in the convergence of the pressure field. While the magnitude of errors in the displacement of the P2b/P1dc element is only slightly lower than that of the P2/P1 element, the magnitude of error in the pressure field obtained with the P2b/P1dc element is even higher than that of the Q1/P0 element, and at least an order of magnitude higher than that of the P2/P1 element. The error magnitude of the pressure field obtained with the P2b/P1dc element is almost two orders higher and the error magnitude of stress is one order of magnitude higher when compared with the P3/P1dc element, indicating a subpar performance of the P2b/P1dc element despite a substantial increase in the number of pressure DOFs when compared with the Q1/P0 and P2/P1 elements and while having the same number of pressure DOFs as that of the P3/P1dc element. The performance of the P3/P1dc element is substantially superior to that of the P2b/P1dc element although both elements have the same number of pressure DOFs.

The subpar performance of the P2b/P1dc element can be further understood through warped plots of the pressure field obtained. As shown in Fig. 7, the pressure field obtained with the P2b/P1dc element is erratic as opposed to the smooth pressure fields obtained with the P2/P1 and P3/P1dc elements.

5.1.2. *Composite thick-walled cylinder*

Similar convergence studies are conducted for the thick-walled cylinder made of two materials, referred to as the *composite cylinder* henceforth, using five meshes shown in Fig. 8. Graphs of error norms are shown in Figs. 9 and 10 for two different values of Poisson's ratio for the same values of Young's moduli, $E_1 = 200$ MPa and $E_2 = 20$ MPa. The graphs show the expected rate of convergence for displacement, pressure and stress fields for the Q1/P0, P2b/P1dc and P3/P1dc elements. However, the rate of convergence for the P2/P1 element deteriorates substantially in all the fields: the displacement convergence rate is *one* instead of *three* and pressure and stress converge at a rate of 0.5 instead of *two*. This drop in convergence rates for the P2/P1 element is due to the fact that the pressure nodes (and hence DOFs) are continuous across the elements. Therefore, the default implementation of the P2/P1 element is incapable of capturing the pressure jumps across material interfaces, see Fig. 11(b). On the contrary, Q1/P0, P2b/P1dc and P3/P1dc elements capture the pressure jumps accurately. However, within each cylindrical domain, the pressure field obtained with the P2b/P1dc element (see Fig. 11(c)) shows the same erratic behaviour as observed in the case of the simple

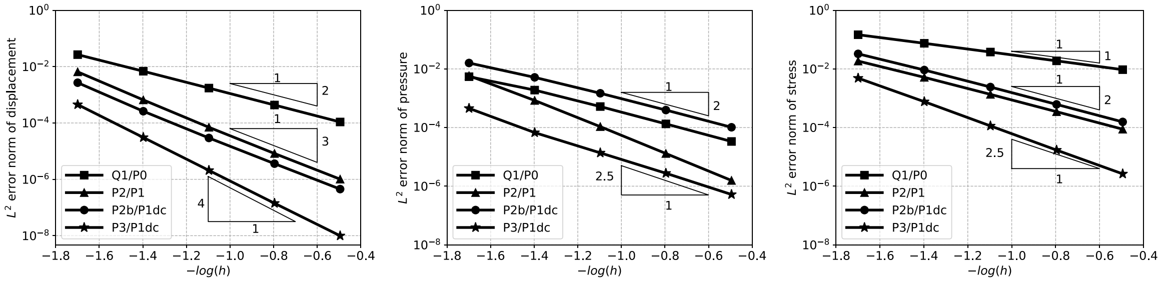

(a) (b) (c)

Fig. 5. Simple thick-walled cylinder: L^2 relative error norms of displacement, pressure and stress for $E = 200$ MPa and $\nu = 0.3$.

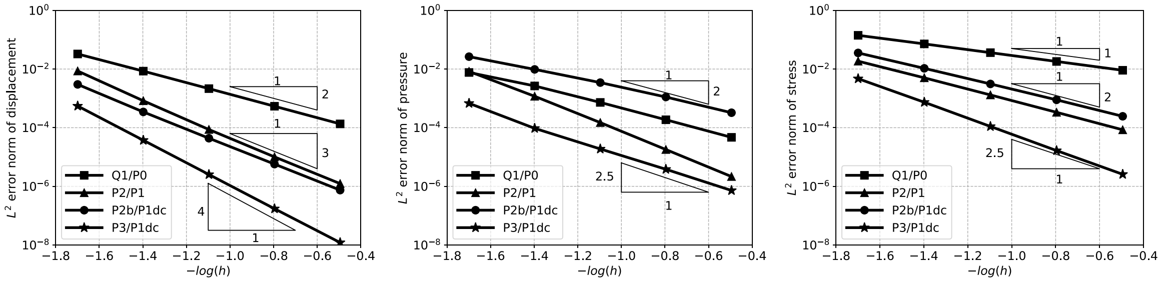

(a) (b) (c)

Fig. 6. Simple thick-walled cylinder: L^2 relative error norms of displacement, pressure and stress for $E = 200$ MPa and $\nu = 0.5$.

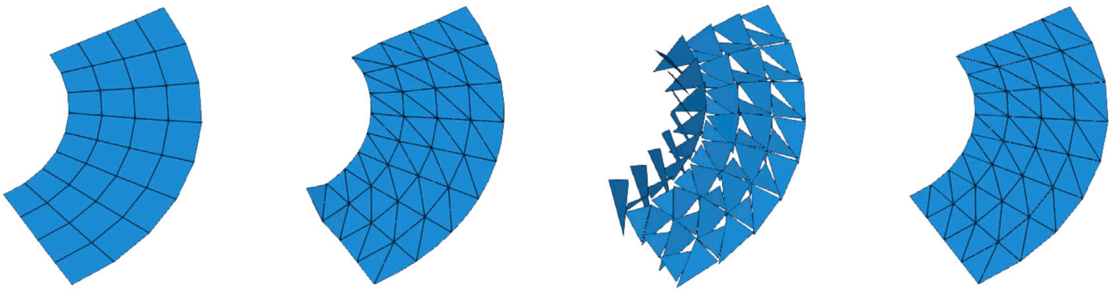

(a) Q1/P0, 4x8 mesh (b) P2/P1, mesh 2 (c) P2b/P1dc, mesh 2 (d) P3/P1dc, mesh 2

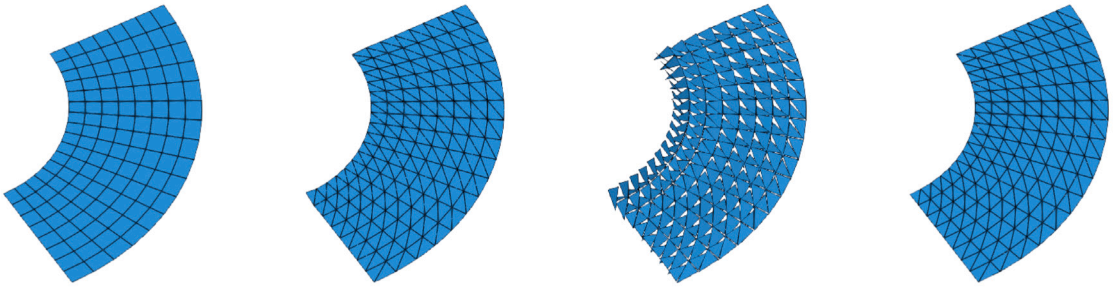

(e) Q1/P0, 8x16 mesh (f) P2/P1, mesh 3 (g) P2b/P1dc, mesh 3 (h) P3/P1dc, mesh 3

Fig. 7. Simple thick-walled cylinder: warped plots of pressure (by a factor of 1000) obtained with Q1/P0, P2/P1, P2/P1dc and P3/P1dc elements for $E = 200$ MPa and $\nu = 0.5$.

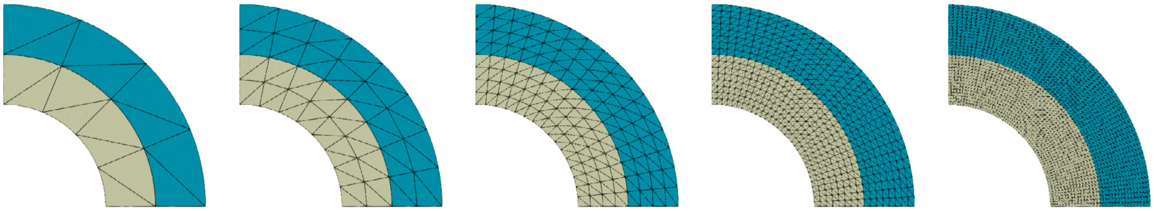

(a) mesh 1 (b) mesh 2 (c) mesh 3 (d) mesh 4 (e) mesh 5

Fig. 8. Composite thick-walled cylinder: meshes used for the analysis.

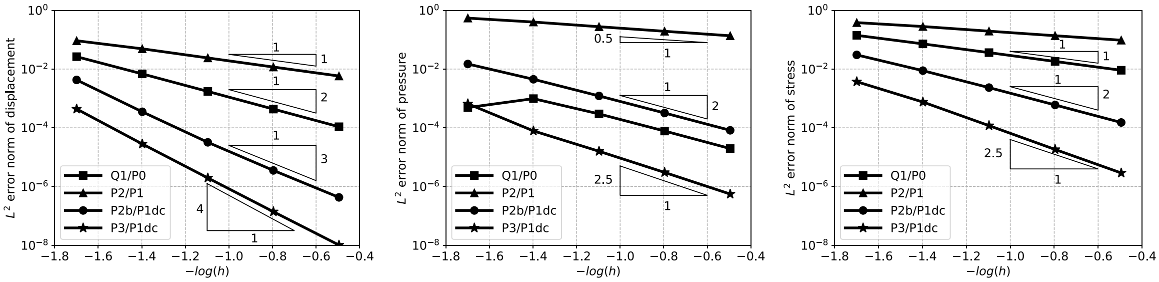

(a) (b) (c)

Fig. 9. Composite thick-walled cylinder: L^2 relative error norms of displacement, pressure and stress for $E_1 = 200$ MPa, $E_2 = 20$ MPa and $\nu_1 = \nu_2 = 0.3$.

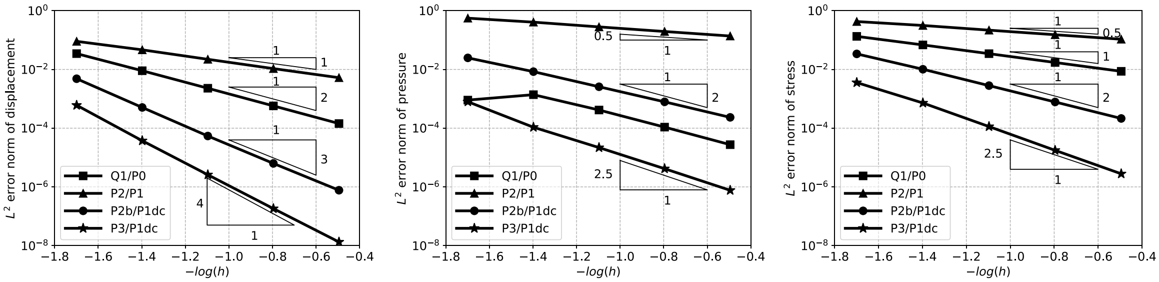

(a) (b) (c)

Fig. 10. Composite thick-walled cylinder: L^2 relative error norms of displacement, pressure and stress for $E_1 = 200$ MPa, $E_2 = 20$ MPa and $\nu_1 = \nu_2 = 0.5$.

cylinder. The pressure field obtained with the P3/P1dc element is not only discontinuous at the material interface but also smoother within each domain, as shown in Fig. 11(d).

At this point, it is worth highlighting the superior accuracy of the P3/P1dc element in all the fields. With only three additional nodes for the displacement field when compared with the P2b/P1dc element, the convergence rates of displacement and pressure (and stress) increase, respectively, by an order of *one* and 0.5, and at the same time the magnitudes of errors in all the quantities are lower by at least one order when compared with the P2b/P1dc element. The additional computational cost of the P3/P1dc element is worth it when we consider the accuracy of the results obtained, particularly pressure and stress fields.

5.2. Thick-walled composite sphere under internal pressure

We consider the thick-walled composite sphere to study the performance 3D versions of P2/P1, P2b/P1dc and P3/P1dc elements. The radii of the spheres are 100, 150 and 200 mm. Due to the symmetry, only 1/8th of the sphere with symmetry boundary conditions is considered for the analysis. The Young's moduli of the inner and outer cylinders, respectively, are $E_1 = 200$ MPa and $E_2 = 20$ MPa, and the Poisson's ratio is $\nu_1 = \nu_2 = 0.5$. Four meshes shown in Fig. 12 are used for the analysis, and the graphs of displacement, pressure and stress fields are shown in Fig. 13. As shown, the error norms for all three element types show the

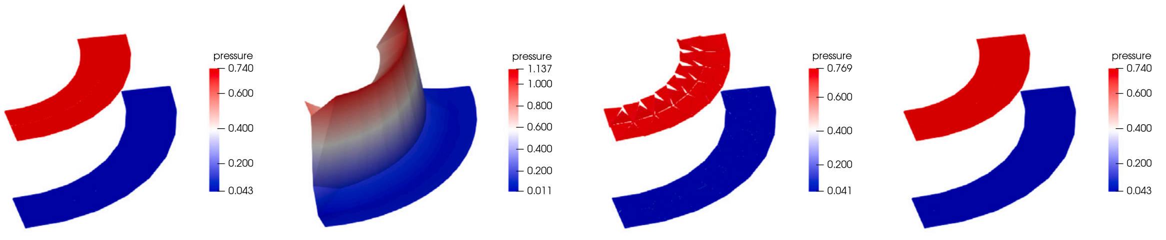

(a) Q1/P0, 4x8 mesh (b) P2/P1, mesh 2 (c) P2b/P1dc, mesh 2 (d) P3/P1dc, mesh 2

Fig. 11. Composite thick-walled cylinder: contours of plots of pressure (warped by a factor of 100) obtained with different element types for $E_1 = 200$ MPa, $E_2 = 20$ MPa and $\nu_1 = \nu_2 = 0.5$.

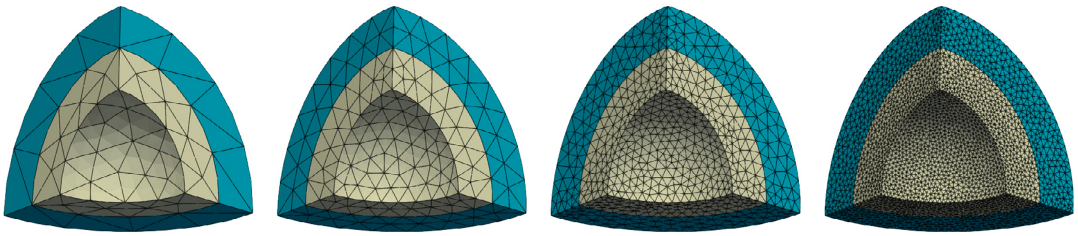

(a) mesh 1 (b) mesh 2 (c) mesh 3 (d) mesh 4

Fig. 12. Thick-walled composite sphere: meshes used for the analysis.

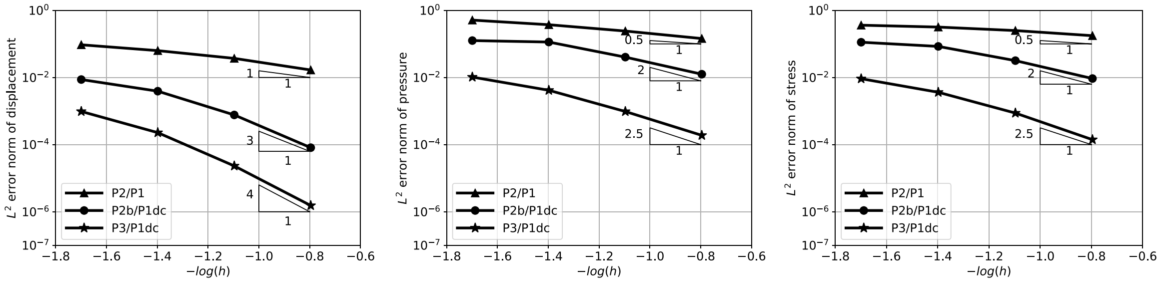

(a) (b) (c)

Fig. 13. Thick-walled composite sphere: L^2 relative error norms of displacement, pressure and stress for $E_1 = 200$ MPa, $E_2 = 20$ MPa, and $\nu_1 = \nu_2 = 0.5$.

same trend as observed in the 2D case. The P2/P1 element fails to capture the pressure jumps accurately, and the P3/P1dc element shows superior performance when compared with the P2b/P1dc element, yielding a higher convergence rate and lower magnitude of errors. The contour plots of pressure presented in Fig. 14 for mesh 2 show the inability of the P2/P1 element to accurately capture pressure jumps at the interface, and smoother pressure fields along with accurate pressure jumps obtained with the P3/P1dc element.

5.3. Cook's membrane in 2D

We now consider the original and modified cases of the popular Cook's membrane benchmark. The first case is the Cook's membrane problem with a single material, and the second case is the modified one with two materials with different material properties, as shown in Fig. 15.

5.3.1. Cook's membrane with single material

For this case, Young's modulus is $E = 240.565$ MPa and Poisson's ratio is $\nu = 0.4999$. As shown in Fig. 16, five meshes are used for the analysis using triangular elements. Mapped meshes with corresponding number of elements per side are used for the Q1/P0

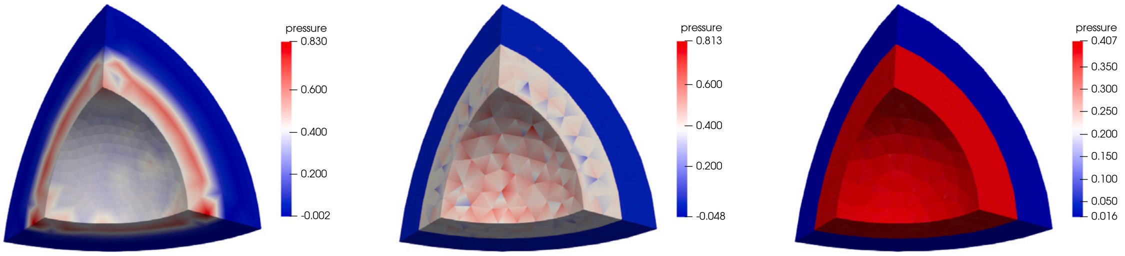

(a) P2/P1 (b) P2b/P1dc (c) P3/P1dc

Fig. 14. Thick-walled composite sphere: contours of plots of pressure obtained with different element types using mesh 2.

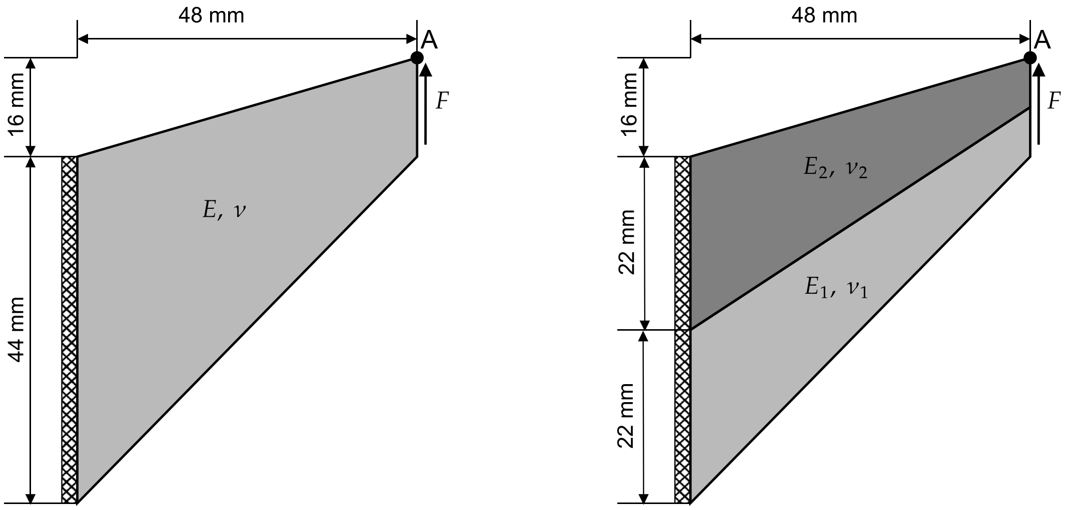

(a) (b)

Fig. 15. Cook's membrane: setup of (a) single material case and (b) two material case.

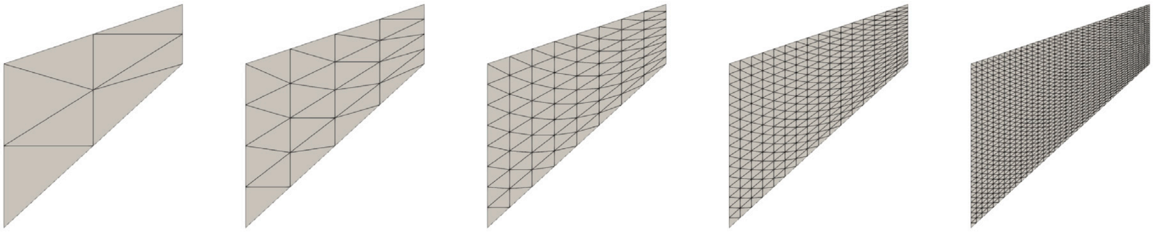

(a) (b) (c) (d) (e)

Fig. 16. Cook's membrane with a single material: meshes used for the analysis.

element. Only five load steps are used for the simulations with the Neo-Hookean model. The Y-displacement of point A with mesh refinement using different element types is shown in Fig. 17 for linear elastic and Neo-Hookean materials. All the element types converge with mesh refinement and match well with the reference values from the literature. Although the solution with the Q1/P0 element converges with mesh refinement, the pressure field obtained shows the well-known checkerboard pattern, see Fig. 18. The pressure field obtained with P2/P1 and P3/P1dc elements is smoother than that obtained with the P2b/P1 element, consistent with the results obtained in the thick-walled cylinder example.

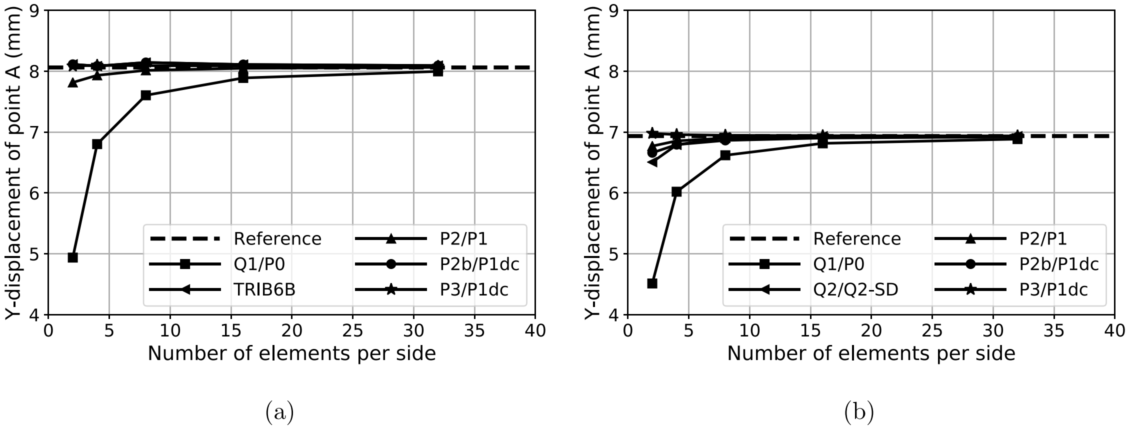

Fig. 17. Cook's membrane with a single material: convergence of Y-displacement of point A for $E = 240.565$ MPa and $\nu = 0.4999$ with (a) linear elastic material and Neo-Hookean material. Reference values are from Kadapa et al. [15].

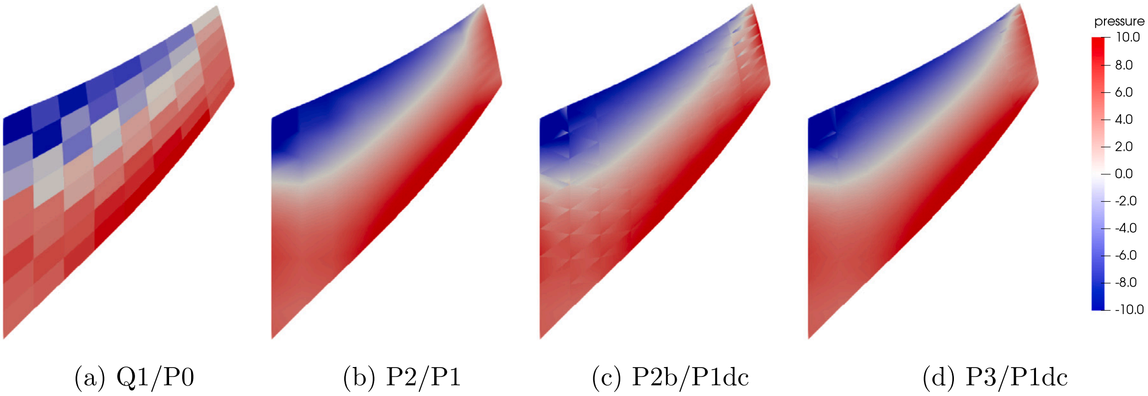

(a) Q1/P0 (b) P2/P1 (c) P2b/P1dc (d) P3/P1dc

Fig. 18. Cook's membrane with a single material: contours of pressure obtained with the Neo-Hookean model and different element types for $\nu = 0.4999$.

5.3.2. *Cook's membrane with two materials*

For the two-material version, two cases are considered. The Young's modulus and Poisson's ratio for case 1 are: $E_1 = 250$ MPa, $E_2 = 2.5$ MPa, $\nu_1 = 0.5$ and $\nu_2 = 0.5$. For case 2, $\nu_2 = 0.2$ with other parameters being the same as those of case 1. The load value is $F = 1$ N/mm for both cases.

The convergence of the Y-displacement of point A with respect to mesh refinement, as shown in Fig. 19, follows the same trend for both cases. Interestingly, the P2/P1 and P3/P1dc elements converge from above, while Q1/P0 and P2b/P1dc elements converge from below. Although the displacement solution obtained with all elements converges with mesh refinement, the pressure field obtained with the P2/P1 element differs significantly at the interface due to the continuity of the pressure DOFs, see Fig. 20. Even though P2b/P1dc and P3/P1dc elements capture the pressure jump accurately, the pressure field obtained with the P3/P1dc element is smoother within each domain.

5.4. *Block under compression in 3D*

5.4.1. *Block with a single material*

We first consider the benchmark example of a homogeneous block under compression. Due to the symmetry of the boundary and loading conditions, a quarter portion of the block with symmetry boundary conditions is modelled, as shown in Fig. 21(a). The material model is the Neo-Hookean model with Young's modulus of 240.565 MPa and a Poisson's ratio of 0.4999. The problem is studied using five meshes shown in Fig. 22, and the Z-displacement of point A as the percentage of compression is plotted in Fig. 21(b) for different elements. As shown, accurate results are obtained with coarse meshes using P2b/P1dc and P3/P1dc elements. From the contour plots of pressure presented in Fig. 23, we can see that the pressure field obtained with the P3/P1dc element is smoother than that of the P2b/P1dc element.

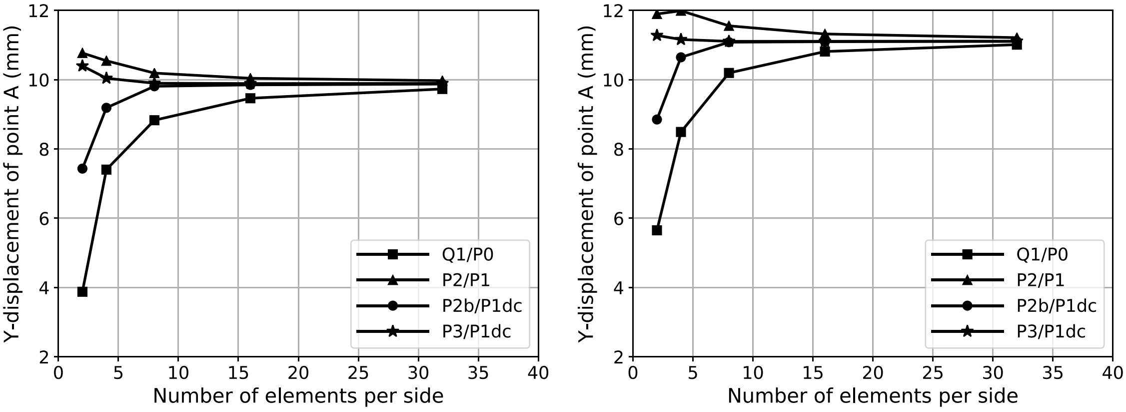

(a) (b)

Fig. 19. Cook's membrane with two materials: convergence of Y-displacement of point A for $E_1 = 250$ MPa, $E_2 = 2.5$ MPa, $\nu_1 = 0.5$ and (a) $\nu_2 = 0.5$ and (b) $\nu_2 = 0.2$.

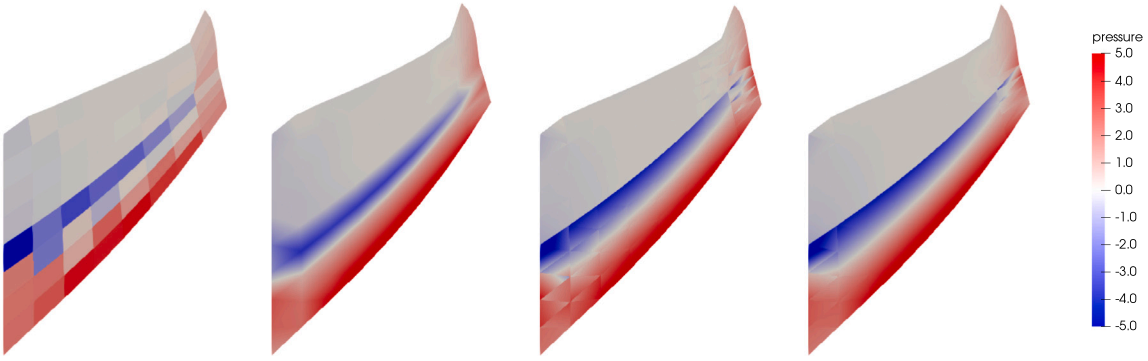

(a) Q1/P0 (b) P2/P1 (c) P2b/P1dc (d) P3/P1dc

Fig. 20. Cook's membrane with two materials: contours of pressure obtained with the linear elastic material model and different element types.

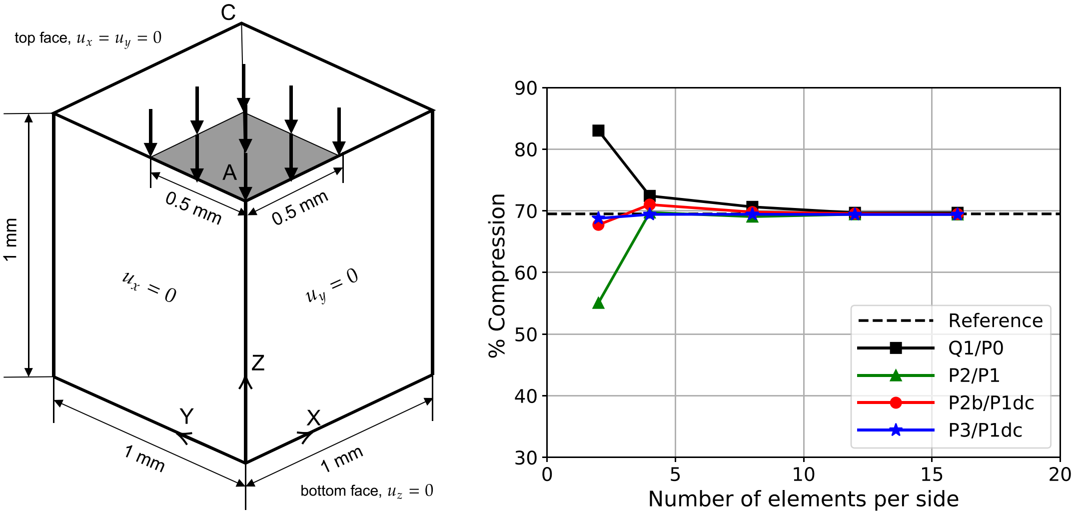

(a) (b)

Fig. 21. Block under compression: (a) problem setup, and (b) comparison of compression level obtained with different element types.

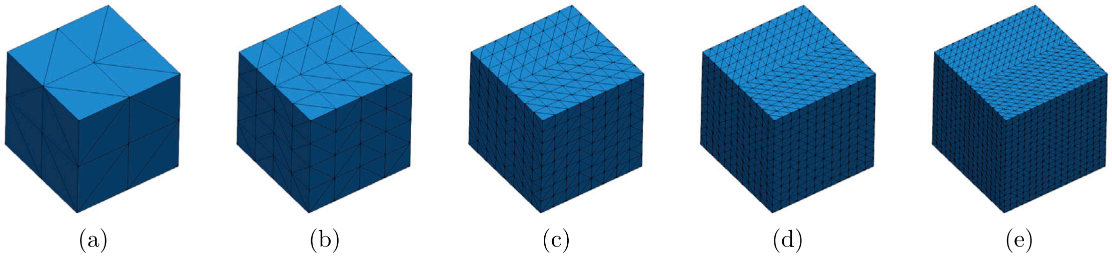

Fig. 22. Block under compression: plots of meshes with 2, 4, 8, 12 and 16 elements per side.

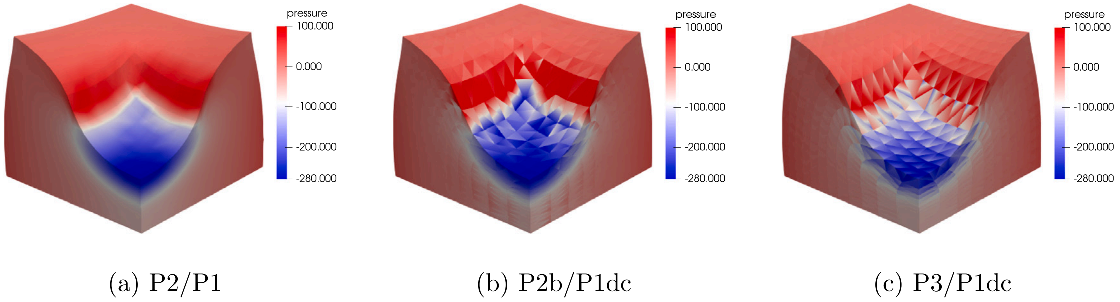

(a) P2/P1 (b) P2b/P1dc (c) P3/P1dc

Fig. 23. Block under compression: contour plots of pressure obtained with different element types for the mesh with 12 elements per side.

Table 1
Multilayer block: material properties of different layers.

Layer	Material model	Material properties
Layer 1	Mooney–Rivlin	C_{10} = 541.552 Pa, C_{01} = 100 Pa, κ = 10000 Pa
Layer 2	Neo-Hookean	μ = 320.776 Pa, κ = 32000 Pa
Layer 3	Neo-Hookean	μ = 160.388 Pa, κ = 16000 Pa
Layer 4	Neo-Hookean	μ = 80.194 Pa, κ = 8000 Pa

5.4.2. Block with four layers

Next, we consider the block with four layers from Wu et al. [12]. The setup of the problem is shown in Fig. 24. The material properties of each layer are tabulated in Table 1. The analysis is performed using two meshes shown in Fig. 24 with P2/P1, P2b/P1dc and P3/P1dc elements. The first and second meshes consist of 627 and 3742 elements, respectively. The number of nodes for the respective meshes are 1131 and 5935 for the P2 element, 1758 and 9677 for the P2b element, and 3475 and 18935 for the P3 element. The load is applied in five uniform increments. The deformed shapes are presented in Fig. 25. The graphs of Z-displacement along the diagonal like AC presented in Fig. 26 show that the results obtained with different elements match well with the reference solution obtained with finer meshes (48004 nodes) in Wu et al. [12]. The contour plots of the pressure field in Fig. 27 show that P2b/P1dc and P3/P1dc elements capture the pressure jumps accurately while the P2/P1 element fails to do so.

5.5. Twisting of a layered column

We now consider the torsion of a square column with four layers. The problem setup and the meshes used for the analysis are presented in Fig. 28. The material model is the incompressible Neo-Hookean with E = 170 MPa for layers 1 and 3 and E = 17 MPa for layers 2 and 4. The simulations are carried out for one full rotation with a load step of 9 degrees. The deformed shapes and contour plots of pressure obtained with the different element types at three different load steps are presented in Fig. 29. While there is a negligible difference in the deformed shapes, the pressure field obtained with the P3/P1dc element is smoother within the individual domains when compared with the P2b/P1dc element.

The wall times to complete 40 load steps with P2/P1, P2b/P1dc and P3/P1dc elements are, respectively, 75, 87 and 510 s using the MUMPS direct solver on a single processor. It is understandable that P3/P1dc elements are computationally more expensive than the P2/P1 and P2b/P1dc elements; however, the accuracy of results is substantially higher. P2b/P1dc element does offer a compromise between the accuracy and computational cost while accurately maintaining the pressure and stress jumps across the

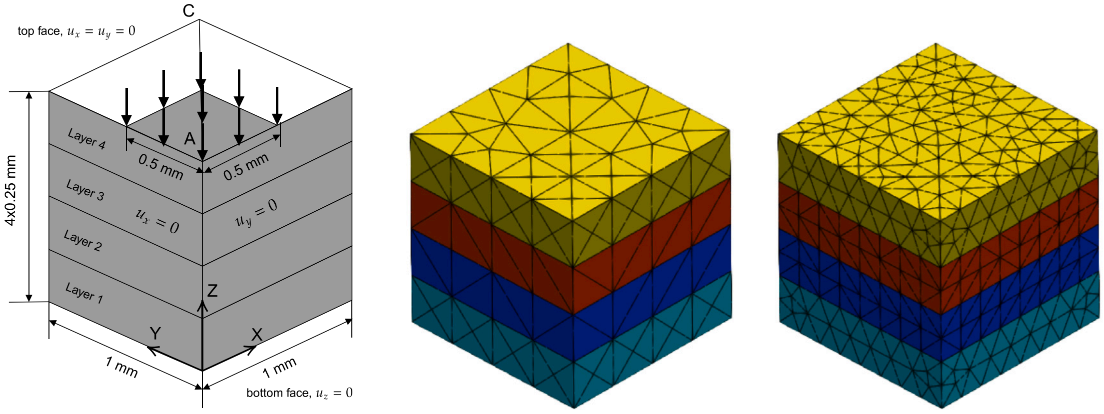

(a) Geometry and BCs (b) Mesh 1 (c) Mesh 2

Fig. 24. Multilayer block: problem setup and meshes used.

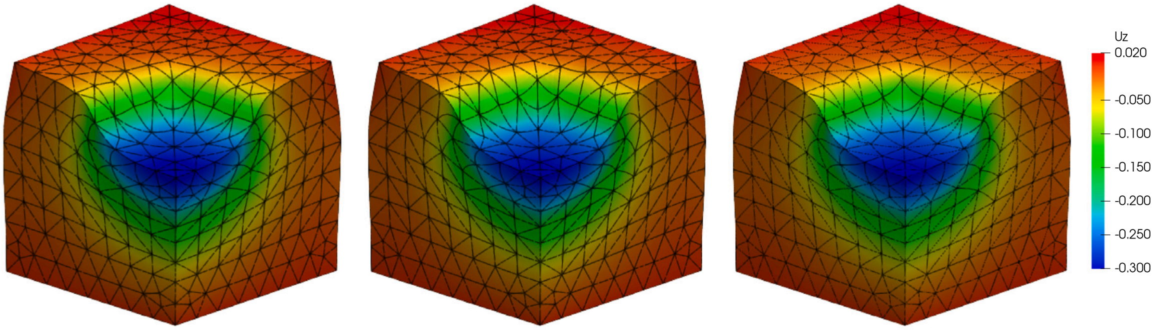

(a) P2/P1 (b) P2b/P1dc (c) P3/P1dc

Fig. 25. Multilayer block: deformed shapes and contour plots of the Z component of displacement obtained with different elements.

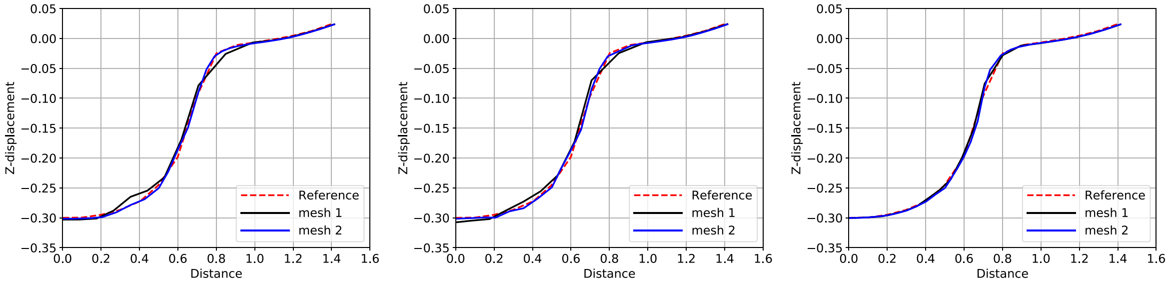

(a) P2/P1 (b) P2b/P1dc (c) P3/P1dc

Fig. 26. Multilayer block: comparison of Z-displacement along the diagonal like AC obtained with P2/P1, P2b/P1dc and P3/P1dc elements against the reference solution from [12].

material interfaces; however, the accuracy of pressure fields obtained within individual domains is subpar when compared with the P3/P1dc element.

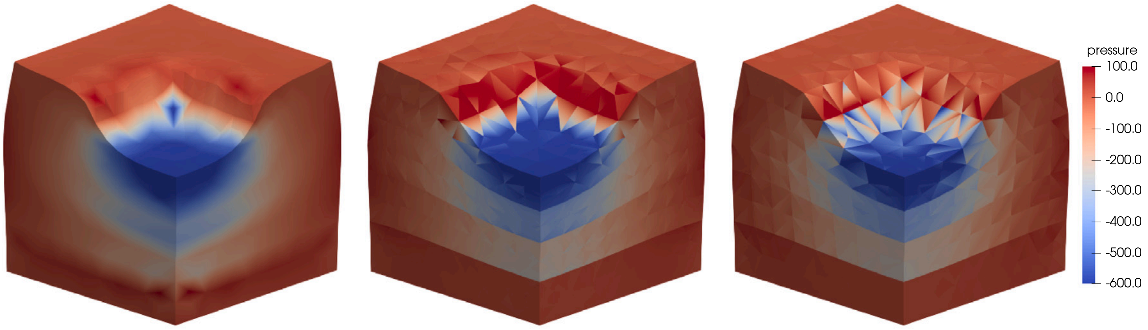

(a) P2/P1 (b) P2b/P1dc (c) P3/P1dc

Fig. 27. Multilayer block: contour plots of pressure obtained with different element types with mesh 2.

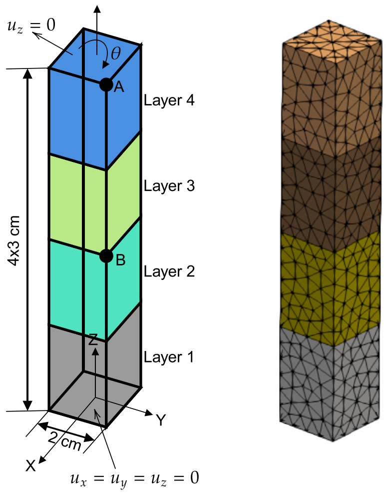

(a) (b)

Fig. 28. Twisting of a layered column: (a) problem setup and (b) the mesh used for the simulation.

5.6. *Twisting of a fibre-reinforced soft tissue*

We now consider a soft tissue sample of length 5 mm and diameter 2 mm that is reinforced with fibres of diameter 0.4 mm placed at $(\pm 0.3, \pm 0.3)$ mm, as depicted in Fig. 30. The material model is the incompressible Neo-Hookean model with the shear modulus of 1 MPa and 10 MPa, respectively, for the matrix and fibre. The problem is simulated with Q1/P0, P2b/P1dc and P3/P1dc elements using the meshes shown in Fig. 30 for a rotation of 360 degrees using increments of 9 degrees. The solution obtained with the Q1/P0 element is used as the reference. The deformed shapes at 180 and 360 degrees obtained with the Q1/P0 and P3/P1dc elements are shown in Fig. 31. The contour plots of pressure presented in Figs. 32 and 33 clearly show that the pressure field obtained with the P2b/P1dc element is significantly poor when compared with the P3/P1dc element.

5.7. *Particle-filled soft composite*

As the last example, we consider a soft matrix filled with particles. This example demonstrates the need for accurate and robust tetrahedral elements since the generation of meshes with hexahedral elements for such problems is cumbersome. The matrix is a cube of side length 1 mm and is filled with six spherical particles of radii 0.1, 0.12, 0.1, 0.12, 0.1 and 0.12 mm with their respective centres at (0.25,0.6,0.1), (0.6, 0.5, 0.3), (0.6, 0.3, 0.7), (0.3, 0.3, 0.3), (0.3, 0.7, 0.3) and (0.7, 0.7, 0.7). The material model for the matrix is incompressible Mooney–Rivlin with $c_1 = 0.375$ and $c_2 = 0.125$ MPa, and that for the particles is incompressible Neo-Hookean with $\mu = 100$ MPa. The face at $X = 0$ is fixed, and a displacement of $(0.8, 0, 0)$ mm is applied on the face at $X = 1$ mm in increments of 0.1 mm. The mesh used for the simulation is shown in Fig. 34.

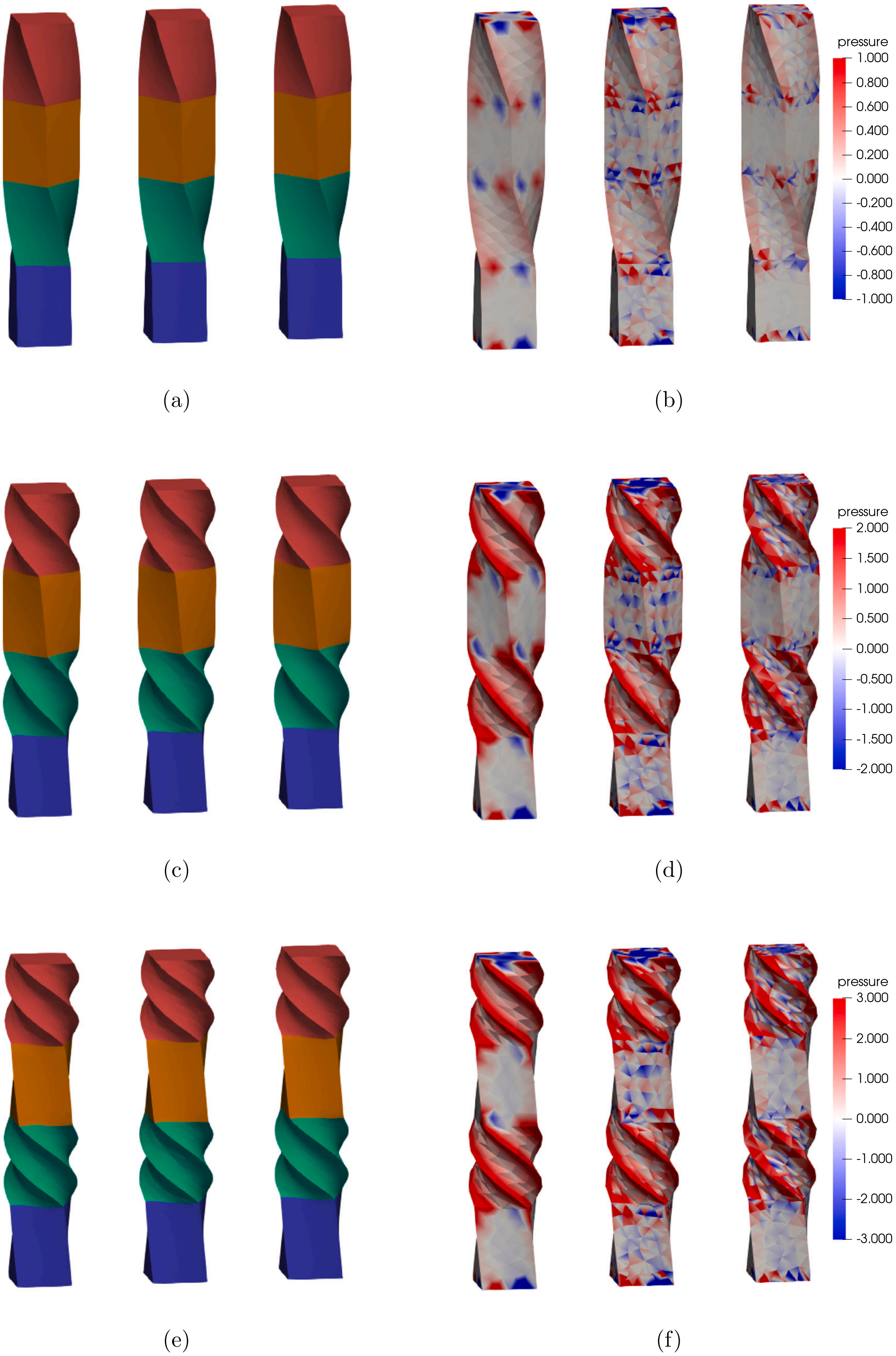

Fig. 29. Twisting of a layered column: deformed shapes and contour plots of pressure at 90 degrees ((a) and (b)), 270 degrees ((c) and (d)) and 360 degrees ((e) and (f)). In each subfigure: (Left) P2/P1, (Centre) P2b/P1dc and (Right) P3/P1dc.

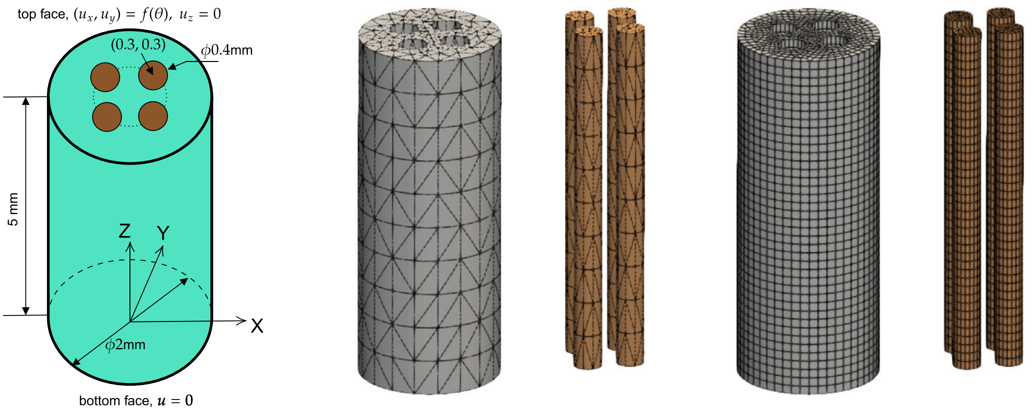

(a) Problem setup (b) Tetrahedral mesh (c) Hexahedral mesh

Fig. 30. Twisting of a fibre-reinforced soft tissue: problem setup and meshes used for the simulation.

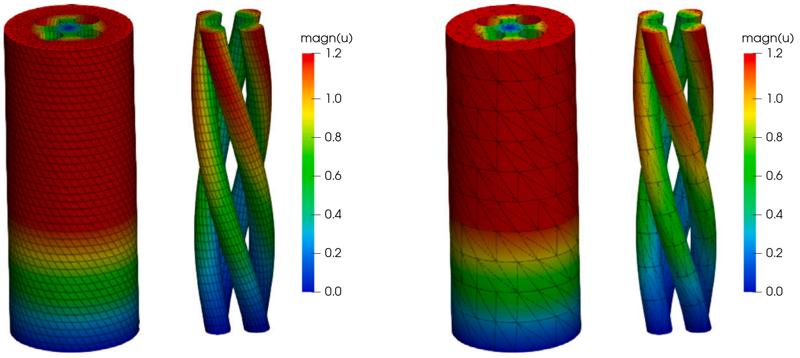

(a) Q1/P0 at 180 degrees (b) P3/P1dc at 180 degrees

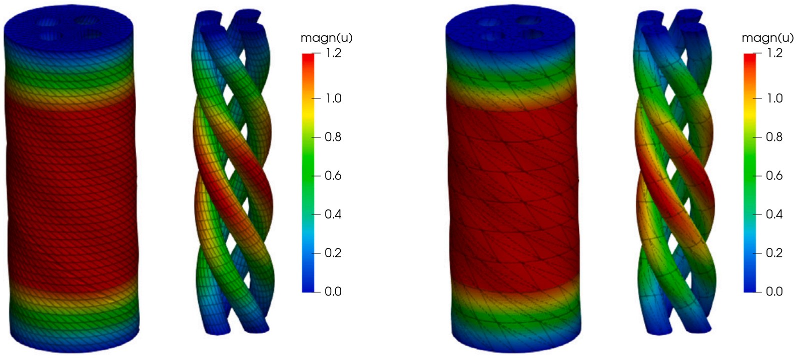

(c) Q1/P0 at 360 degrees (d) P3/P1dc at 360 degrees

Fig. 31. Twisting of a fibre-reinforced soft tissue: deformed shapes and contour plots of displacement magnitude.

There is a negligible difference in the displacements obtained with the P2b/P1dc and P3/P1dc elements. The deformed shapes obtained with the P3/P1dc element at 0.2 mm and 0.8 mm of applied displacement are shown in Fig. 35. The pressure fields obtained with P2b/P1dc and P3/P1dc elements show drastic differences, as presented in Figs. 36 and 37. The pressure fields obtained with the

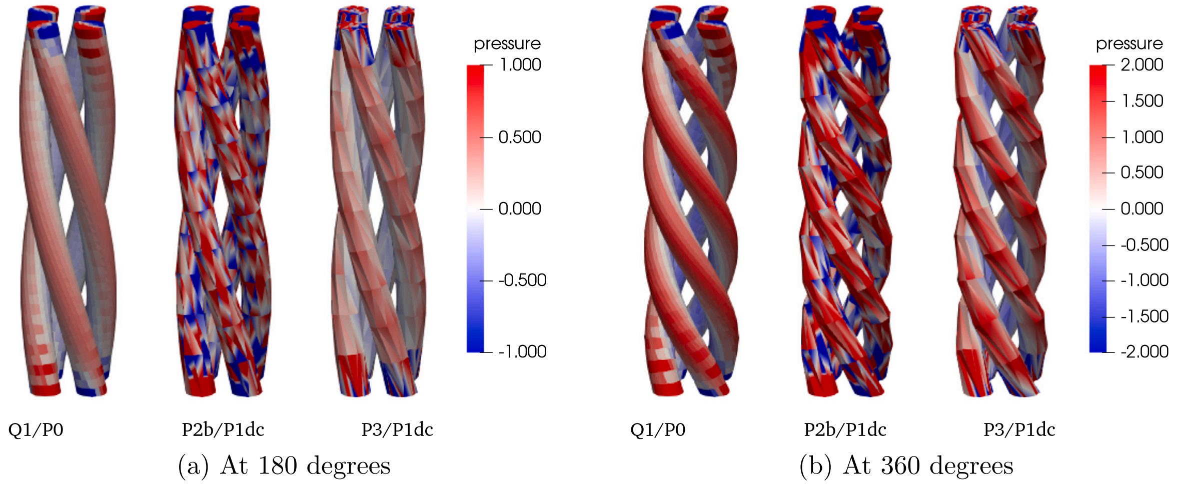

(a) At 180 degrees (b) At 360 degrees

Fig. 32. Twisting of a fibre-reinforced soft tissue: contour plots of pressure for the fibres.

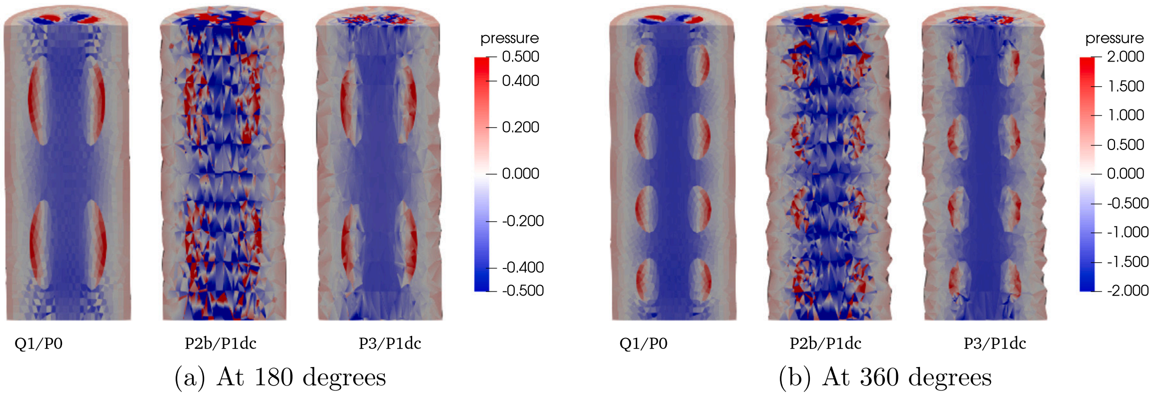

(a) At 180 degrees (b) At 360 degrees

Fig. 33. Twisting of a fibre-reinforced soft tissue: contour plots of pressure for the clipped domains.

P3/P1dc element are much smoother than those of the P2b/P1dc element, indicating better accuracy observed in the thick-walled cylinder and sphere examples with linear elasticity.

6. Conclusions

We have assessed the performance of discontinuous pressure spaces based on triangular and tetrahedral elements in the context of mixed displacement–pressure formulation for the simulation of multimaterial problems in linear and nonlinear elasticity. The novel contribution of the present work is the adaptation of P2b/P1dc and P3/P1dc elements and extensive studies of their relative advantages and disadvantages for problems in linear and nonlinear elasticity. The accuracy of different elements in accurately resolving pressure jumps across material interfaces, as well as in capturing pressure fields within the individual material domains, is assessed using several numerical examples.

The key observations from the results obtained in the present work are:

- The P2/P1 element, without any additional preprocessing, fails to capture pressure jumps across material interfaces due to the continuity of pressure nodes/DOFs across element edges/faces.
- The magnitudes of error norms in pressure obtained with the P2b/P1dc element are higher than those obtained with the Q1/P0 element despite the P2b/P1dc element having significantly higher pressure DOFs.
- For the single material case, converting the P2/P1 element to the P2b/P1dc element by adding an extra node with a cubic bubble function does not lower the displacement error norm significantly. However, surprisingly, the P2b/P1dc element yields pressure fields of substantially poor quality despite a significant increase in pressure DOFs.
- Even though the P2b/P1dc element resolves the pressure jumps across material interfaces accurately, the accuracy of pressure fields within the individual domain is poor. Despite having the same number of pressure DOFs, the magnitudes of error in

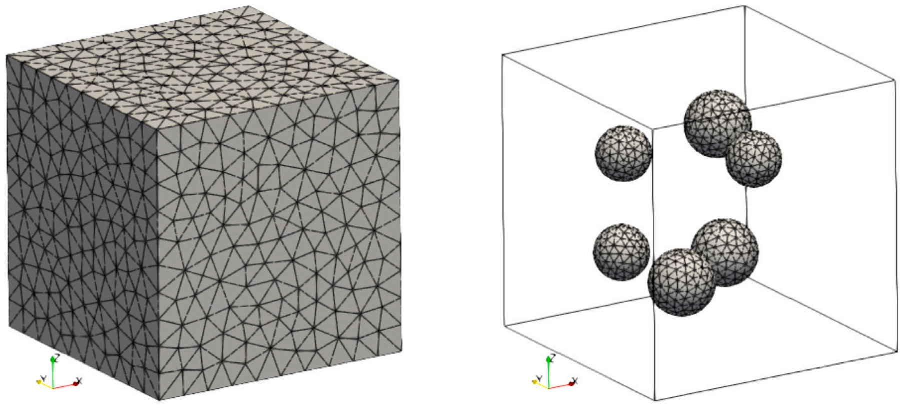

(a) (b)

Fig. 34. Particle-filled composite: mesh used for the simulation.

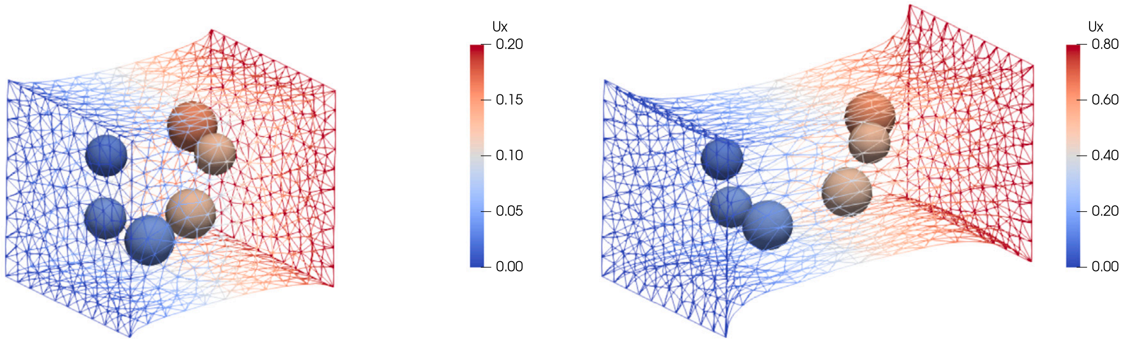

(a) At 0.2 mm (b) At 0.8 mm

Fig. 35. Particle-filled composite: deformed shapes at 0.2 mm and 0.8 mm of applied displacement obtained with the P3/P1dc element.

pressure obtained with the P2b/P1dc element are about two orders of magnitude higher when compared with the P3/P1dc element. The superior accuracy of the P3/P1dc element is evident in the smoother pressure fields obtained with it, as shown with the warped plots of the pressure field for the thick-walled cylinder example. These differences in the accuracy have a substantial effect on the pressure fields obtained for the nonlinear elasticity problems, as demonstrated by the examples of twisting of a layered column and fibre-reinforced soft tissue.

- While the computational cost of the P3/P1dc element is higher than that of the P2b/P1dc element, the accuracy of results obtained with P3/P1dc is substantially better.

In conclusion, the present work offers significant insights into the performance of Q1/P0, P2/P1, P2b/P1dc and P3/P1dc elements for simulating multimaterial problems in linear and nonlinear elasticity. While the Q1/P0 element is reasonably accurate and competitive in terms of performance, the difficulty of mesh hexahedral generation for complex problems makes it less appealing for practical problems. The P2b/P1dc element performs poorly, requiring finer meshes for accurate results. The P3/P1dc yields accurate results using coarse meshes. We hope this work inspires further research on new element technologies for multimaterial problems consisting of incompressible hyperelastic materials.

CRediT authorship contribution statement

Chennakesava Kadapa: Writing – review & editing, Writing – original draft, Visualization, Validation, Software, Project administration, Methodology, Investigation, Formal analysis, Data curation, Conceptualization.

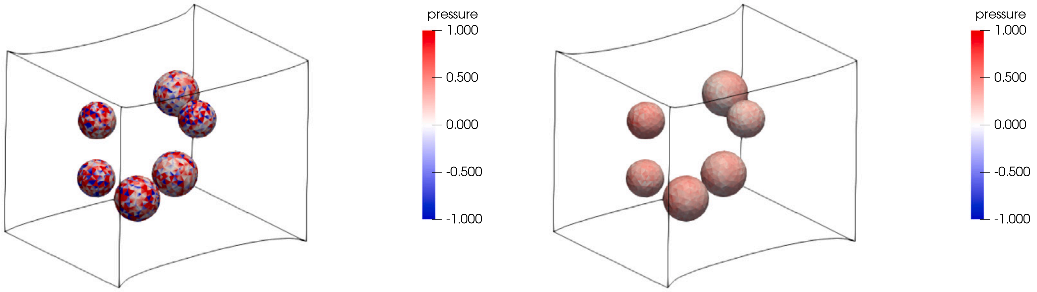

(a) P2b/P1dc at 0.2 mm (b) P3/P1dc at 0.2 mm

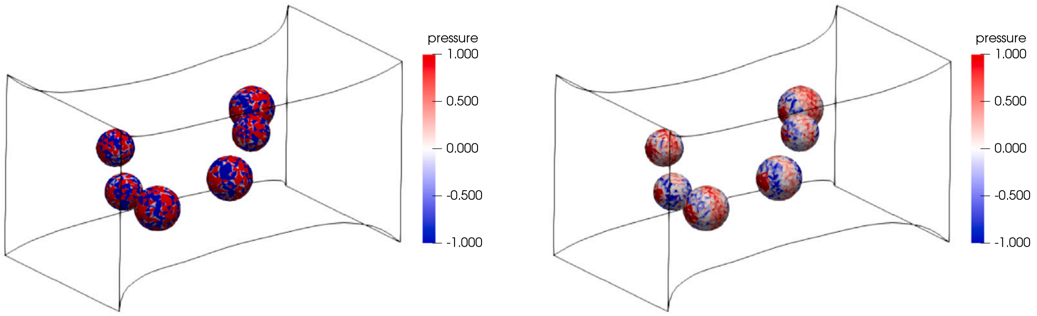

(c) P2b/P1dc at 0.8 mm (d) P3/P1dc at 0.8 mm

Fig. 36. Particle-filled composite: contour plots of pressure for the particles at 0.2 mm and 0.8 mm of applied displacement.

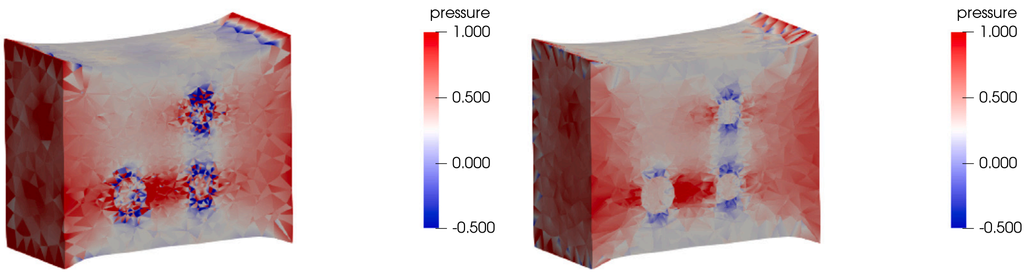

(a) P2b/P1dc at 0.2 mm (b) P3/P1dc at 0.2 mm

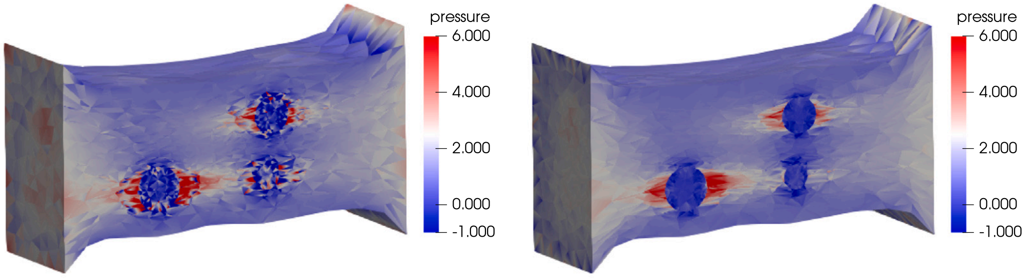

(c) P2b/P1dc at 0.8 mm (d) P3/P1dc at 0.8 mm

Fig. 37. Particle-filled composite: contour plots of pressure on the clipped model (with a plane at 0.4 mm along the Y-axis) at 0.2 mm and 0.8 mm of applied displacement.

Declaration of competing interest

The authors declare that they have no known competing financial interests or personal relationships that could have appeared to influence the work reported in this paper.

Data availability

No data was used for the research described in the article.

Appendix. Analytical solutions for the examples

A.1. Simple thick-walled cylinder

The analytical solution for the simple thick-walled cylinder under internal pressure in plane-strain condition is given as

$$\text{Radial stress}: \sigma_{rr} = A - \frac{B}{r^2}, \tag{A.1}$$

$$\text{Hoop stress}: \sigma_{\theta\theta} = A + \frac{B}{r^2}, \tag{A.2}$$

$$\text{Pressure}: p = \frac{2\,(1+\nu)\,A}{3}, \tag{A.3}$$

$$\text{Hoop strain}: \varepsilon_{\theta\theta} = \frac{1+\nu}{E}\left[[1-2\nu]\;A + \frac{B}{r^2}\right], \tag{A.4}$$

$$\text{Radial displacement}: u_r = \varepsilon_{\theta\theta}\,r = \frac{1+\nu}{E}\left[[1-2\nu]\;A\;r + \frac{B}{r}\right], \tag{A.5}$$

with

$$A = \frac{p_i\,r_i^2}{r_o^2 - r_i^2}, \quad B = A\,r_o^2, \tag{A.6}$$

where r is the radial coordinate, r_i is the inner radius, r_o is the outer radius, p_i is the internal pressure, E is the Young's modulus and ν is the Poisson's ratio.

A.2. Composite thick-walled cylinder

With the expressions for the inner and outer cylinders as

- For the inner cylinder ($r_1 \leq r \leq r_m$)

$$\sigma_{rr_1} = A_1 - \frac{B_1}{r^2}, \tag{A.7}$$

$$\sigma_{\theta\theta_1} = A_1 + \frac{B_1}{r^2}, \tag{A.8}$$

$$p_1 = \frac{2\,(1+\nu_1)\,A_1}{3}, \tag{A.9}$$

$$\varepsilon_{\theta\theta_1} = \frac{1+\nu_1}{E_1}\left[[1-2\nu_1]\;A_1 + \frac{B_1}{r^2}\right], \tag{A.10}$$

$$u_{r_1} = \frac{1+\nu_1}{E_1}\left[[1-2\nu_1]\;A_1\;r + \frac{B_1}{r}\right], \tag{A.11}$$

- For the outer cylinder ($r_m \leq r \leq r_o$)

$$\sigma_{rr_2} = A_2 - \frac{B_2}{r^2}, \tag{A.12}$$

$$\sigma_{\theta\theta_2} = A_2 + \frac{B_2}{r^2}, \tag{A.13}$$

$$p_2 = \frac{2\,(1+\nu_2)\,A_2}{3}, \tag{A.14}$$

$$\varepsilon_{\theta\theta_2} = \frac{1+\nu_2}{E_2}\left[[1-2\nu_2]\;A_2 + \frac{B_2}{r^2}\right], \tag{A.15}$$

$$u_{r_2} = \frac{1+\nu_2}{E_2}\left[[1-2\nu_2]\;A_2\;r + \frac{B_2}{r}\right], \tag{A.16}$$

the unknowns A_1, A_2, B_1 and B_2 can be calculated by solving the following boundary and interface conditions using symbolic computations in Octave.

$$\sigma_{rr_1}(r = r_i) = -p_i, \tag{A.17}$$

$$\sigma_{rr_2}(r = r_o) = 0, \tag{A.18}$$

$$\sigma_{rr_1}(r = r_m) = \sigma_{rr_2}(r = r_m), \tag{A.19}$$

$$\varepsilon_{\theta\theta_1}(r = r_m) = \varepsilon_{\theta\theta_2}(r = r_m). \tag{A.20}$$

The expressions for the unknowns are quite complicated for the generic problem. However, simplified expressions and exact values for the unknowns can be obtained for the given values of $p_i, r_i, r_o, r_m, E_1, E_2, \nu_1$ and ν_2. For example, for $E_1 = 200, E_2 = 20, r_i = 100, r_m = 150, r_o = 200, p_i = 1$ and $\nu_1 = \nu_2$, we get

$$A_1 = \frac{4\,(27 - 20\,\nu_1)}{149 - 114\,\nu_1}, \qquad B_1 = \frac{10000\,(257 - 194\,\nu_1)}{149 - 114\,\nu_1},$$
$$A_2 = \frac{8\,(1 - \nu_1)}{149 - 114\,\nu_1}, \qquad B_2 = \frac{320000\,(1 - \nu_1)}{149 - 114\,\nu_1}$$

A.3. *Composite thick-walled sphere*

Similar to the composite thick-walled cylinder, the solution for the composite thick-walled sphere can be obtained by using the following expressions for the radial stress (σ_{rr},), hoop stress ($\sigma_{\theta\theta}$), pressure (p), hoop strain ($\varepsilon_{\theta\theta}$) and radial displacement (u_r), and using the boundary and interface conditions.

$$\sigma_{rr} = A - \frac{B}{r^3}, \tag{A.21}$$

$$\sigma_{\theta\theta} = A + \frac{B}{r^3}, \tag{A.22}$$

$$p = A, \tag{A.23}$$

$$\varepsilon_{\theta\theta} = \frac{1}{E}\left[[1 - 2\nu]\;A + \frac{1}{2}\,[1 + \nu]\frac{B}{r^3}\right], \tag{A.24}$$

$$u_r = \frac{1}{E}\left[[1 - 2\nu]\;A\,r + \frac{1}{2}\,[1 + \nu]\frac{B}{r^2}\right]. \tag{A.25}$$

References

[1] C. Kadapa, M. Hossain, A robust and computationally efficient finite element framework for coupled electromechanics, Comput. Methods Appl. Mech. Engrg. 372 (2020) 113443.
[2] C. Kadapa, M. Hossain, A unified numerical approach for soft to hard magneto-viscoelastically coupled polymers, Mech. Mater. 166 (2022) 104207.
[3] C. Kadapa, On the advantages of mixed formulation and higher-order elements for computational morphoelasticity, J. Mech. Phys. Solids 148 (2021) 104289.
[4] E.A. de Souza Neto, D. Perić, M. Dutko, D.R.J. Owen, Design of simple low order finite elements for large strain analysis of nearly incompressible solids, Int. J. Solids Struct. 33 (1996) 3277–3296.
[5] J. Bonet, A.J. Burton, A simple average nodal pressure tetrahedral element for incompressible and nearly incompressible dynamic explicit applications, Commun. Numer. Methods Eng. 14 (1998) 437–449.
[6] T. Belytschko, J.S. Ong, W.K. Liu, J.M. Kennedy, Hourglass control in linear and nonlinear problems, Comput. Methods Appl. Mech. Engrg. 43 (1984) 251–276.
[7] J.C. Simo, T.J.R. Hughes, On the variational foundations of assumed strain methods, J. Appl. Mech. 53 (1986) 51–54.
[8] P. Wriggers, J. Korelc, On enhanced strain methods for small and finite deformations, Comput. Mech. 18 (6) (1996) 413–428.
[9] A. Pakravan, P. Krysl, Mean-strain 10-node tetrahedron with energy-sampling stabilization for nonlinear deformation, Internat. J. Numer. Methods Engrg. 111 (2017) 603–623.
[10] C. Jiang, X. Han, Z.-Q. Zhang, G.R. Liu, G.-J. Gao, A locking-free face-based S-FEM via averaging nodal pressure using 4-nodes tetrahedrons for 3D explicit dynamics and quasi-statics, Int. J. Comput. Methods 15 (6) (2018) 1850043.
[11] Y. Onishi, F-Bar aided edge-based smoothed finite element method with 4-node tetrahedral elements for static large deformation elastoplastic problems, Int. J. Comput. Methods 16 (5) (2019) 1840010.
[12] S.-W. Wu, D. Wan, C. Jiang, X. Liu, K. Liu, G.R. Liu, A finite strain model for multi-material, multi-component biomechanical analysis with total Lagrangian smoothed finite element method, Int. J. Mech. Sci. 243 (2023) 108017.
[13] O.C. Zienkiewicz, R.L. Taylor, D.D. Fox, The finite element method for solid and structural mechanics, in: Butterworth and Heinemann, Seventh ed., 2014.
[14] C. Kadapa, Mixed Galerkin and least-squares formulations for isogeometric analysis, (Ph.D. thesis), College of Engineering, Swansea University, 2014.
[15] C. Kadapa, W.G. Dettmer, D. Perić, Subdivision based mixed methods for isogeometric analysis of linear and nonlinear nearly incompressible materials, Comput. Methods Appl. Mech. Engrg. 305 (2016) 241–270.
[16] C. Kadapa, Novel quadratic Bézier triangular and tetrahedral elements using existing mesh generators: Extension to nearly incompressible implicit and explicit elastodynamics in finite strains, Internat. J. Numer. Methods Engrg. 119 (2019) 75–104.
[17] C. Kadapa, M. Hossain, A linearized consistent mixed displacement-pressure formulation for hyperelasticity, Mech. Adv. Mater. Struct. 29 (2) (2020) 267–284.
[18] D. Pantuso, K.-J. Bathe, On the stability of mixed finite elements in large strain analysis of incompressible solids, Finite Elem. Anal. Des. (1997).
[19] M. Chiumenti, Q. Valverde, C.A. de Saracibar, M. Cervera, A stabilized formulation for incompressible elasticity using linear displacement and pressure interpolations, Comput. Methods Appl. Mech. Engrg. 191 (2002) 5253–5264.
[20] A.M. Maniatty, Y. Liu, O. Klaas, M.S. Shephard, Higher order stabilized finite element method for hyperelastic finite deformation, Comput. Methods Appl. Mech. Engrg. 191 (2002) 1491–1503.

[21] K. Xia, H. Yao, A Galerkin/least-square finite element formulation for nearly incompressible elasticity/stokes flow, Appl. Math. Model. 31 (2007) 513–529.
[22] M. Cervera, M. Chiumenti, R. Codina, Mixed stabilized finite element methods in nonlinear solid mechanics. Part I: formulation, Comput. Methods Appl. Mech. Engrg. 199 (2010) 2559–2570.
[23] M. Cervera, M. Chiumenti, R. Codina, Mixed stabilized finite element methods in nonlinear solid mechanics. Part II: strain localization, Comput. Methods Appl. Mech. Engrg. 199 (2010) 2571–2589.
[24] G. Scovazzi, B. Carnes, X. Zeng, S. Rossi, A simple, stable, and accurate linear tetrahedral finite element for transient, nearly, and fully incompressible solid dynamics: a dynamic variational multiscale approach, Internat. J. Numer. Methods Engrg. 106 (2016) 799–839.
[25] T.-H. Huang, C.-L. Chao, A stabilized one-point integrated mixed formulation for finite element and meshfree methods in modeling nearly incompressible materials, Acta Mech. 233 (2022) 1147–1172.
[26] G. Scovazzi, T. Song, X. Zeng, A velocity/stress mixed stabilized nodal finite element for elastodynamics: Analysis and computations with strongly and weakly enforced boundary conditions, Comput. Methods Appl. Mech. Engrg. 325 (2017) 532–576.
[27] N. Abboud, G. Scovazzi, Elastoplasticity with linear tetrahedral elements: A variational multiscale method, Internat. J. Numer. Methods Engrg. 115 (2018) 913–955.
[28] L.P. Franca, T.J.R. Hughes, A.F.D. Loula, I. Miranda, A new family of stable elements for nearly incompressible elasticity based on a mixed Petrov–Galerkin finite element formulation, Numer. Math. 53 (1988) 123–141.
[29] O. Klaas, A. Maniatty, M.S. Shephard, A stabilized mixed finite element method for finite elasticity. Formulation for linear displacement and pressure interpolation, Comput. Methods Appl. Mech. Engrg. 180 (1999) 65–79.
[30] A. Masud, K. Xia, A stabilized mixed finite element method for nearly incompressible elasticity, J. Appl. Mech. 72 (2005) 711–720.
[31] A. Masud, T.J. Truster, L.A. Bergman, A variational multiscale a posteriori error estimation method for mixed form of nearly incompressible elasticity, Comput. Methods Appl. Mech. Engrg. 200 (2011) 3453–3481.
[32] J. Liu, A.L. Marsden, A robust and efficient iterative method for hyper-elastodynamics with nested block preconditioning, J. Comput. Phys. 383 (2019) 72–93.
[33] E. Karabelas, G. Haase, G. Plank, C.M. Augustin, Versatile stabilized finite element formulations for nearly and fully incompressible solid mechanics, Comput. Mech. 65 (2020) 193–215.
[34] N. Thekkethil, S. Rossi, H. Gao, S.I.H. Richardson, B.E. Griffith, X. Luo, A stabilized linear finite element method for anisotropic poroelastodynamics with application to cardiac perfusion, Comput. Methods Appl. Mech. Engrg. 405 (2023) 115877.
[35] I. Castanar, R. Codina, J. Baiges, A stabilized mixed three-field formulation for stress accurate analysis including the incompressible limit in finite strain solid dynamics, Internat. J. Numer. Methods Engrg. 124 (2023) 2341–2366.
[36] R. Rossi, R. Zorrilla, R. Codina, A stabilised displacement-volumetric strain formulation for nearly incompressible and anisotropic materials, Comput. Methods Appl. Mech. Engrg. 377 (2021) 113701.
[37] G. Scovazzi, R. Zorrilla, R. Rossi, A kinematically stabilzed linear tetrahedral finite element for compressible and nearly incompressible finite elasticity, Comput. Methods Appl. Mech. Engrg. 412 (2023) 116076.
[38] K.J. Bathe, Finite Element Procedures, Prentice Hall Inc., New Jersey, 1996.
[39] J.C. Simo, R.L. Taylor, K.S. Pister, Variational and projection methods for the volume constraint in finite deformation elasto-plasticity, Comput. Methods Appl. Mech. Engrg. 51 (1985) 177–208.
[40] M. Crouzeix, P.-A. Raviart, Conforming and Non-confirming finite element methods for solving the stationary Stokes equations, Revue Française d'Automatique Informatique, Recherche Opérationnelle, Mathématique 7 (1973) 33–75.
[41] D. Boffi, F. Brezzi, M. Fortin, Mixed Finite Element Methods and Applications, Springer, 2013.
[42] V. John, Finite Element Methods for Incompressible Flow Problems, Springer, 2010.
[43] P.M. Gresho, R.L. Sani, Incompressible Flow and the Finite Element Method, Volume 2: Isothermal Laminar Flow, Wiley, Chichester, UK, 2000.
[44] C. Kadapa, A novel semi-implicit scheme for elastodynamics and wave propagation in nearly and truly incompressible solids, Acta Mech. 232 (2021) 2135–2163.
[45] C. Truesdell, R. Toupin, The Classical Field Theories, Springer Berlin Heidelberg, Berlin, Heidelberg, 1960, pp. 226–858.
[46] C. Geuzaine, J.-F. Remacle, Gmsh: a three-dimensional finite element mesh generator with built-in pre- and post-processing facilities, Internat. J. Numer. Methods Engrg. 79 (2009) 1309–1331.
[47] Utkarsh. Ayachit, The ParaView Guide: A Parallel Visualization Application, Kitware, 2015.